Evolution of a Surge Cycle of the Bering-Bagley Glacier System from Observations and Numerical Modeling

Thomas Trantow[1] and Ute C. Herzfeld[1]

[1]Department of Electrical, Energy and Computer Engineering, University of Colorado, Boulder, Colorado, USA

Key Points:

- Using a full-Stokes approach informed by satellite observations, a quiescent and surge phase of the BBGS are simulated
- Local bed topography controls the formation of several reservoir areas, which lengthen down-glacier drainage paths during quiescence
- A friction representation for the surge phase is implemented based on observed properties of kinematic surge waves in the BBGS

Corresponding author: Thomas Trantow, `trantow@colorado.edu`

Abstract

The Bering-Bagley Glacier System (BBGS), Alaska, Earth's largest temperate surging glacier, surged in 2008-2013. We use numerical modeling and satellite observations to investigate how surging in a large and complex glacier system differs from surging in smaller glaciers for which our current understanding of the surge phenomenon is based. With numerical simulations of a long quiescent phase and a short surge phase in the BBGS, we show that surging is more spatiotemporally complex in larger glaciers with multiple reservoir areas forming during quiescence which interact in a cascading manner when ice accelerates during the surge phase.

For each phase, we analyze the simulated elevation-change and ice-velocity pattern, infer information on the evolving basal drainage system through hydropotential analysis, and supplement these findings with observational data such as CryoSat-2 digital elevation maps. During the quiescent simulation, water drainage paths become increasingly lateral and hydropotential wells form indicating an expanding storage capacity of subglacial water. These results are attributed to local bedrock topography characterized by large subglacial ridges that dam the down-glacier flow of ice and water. In the surge simulation, we model surge evolution through Bering Glacier's trunk by imposing a basal friction representation that mimics a propagating surge wave. As the surge progresses, drainage efficiency further degrades in the active surging-zone from its already inefficient, end-of-quiescence state. Results from this study improve our knowledge of surging in large and complex systems which generalizes to glacial accelerations observed in outlet glaciers of Greenland, thus reducing uncertainty in modeling sea-level rise.

Plain Language Summary

The Bering-Bagley Glacier System (BBGS), Alaska, Earth's largest temperate surging glacier, recently surged in 2008-2013. A surge glacier cycles between a long period of normal flow and a short period of accelerated flow where large-scale deformations, such as crevasses, occur. This paper focuses on investigating a surge in a large and complex system rather than a small glacier where most studies on surges have been conducted. We use a numerical model to simulate glacier evolution for both the quiescent phase and the initial surge phase of the BBGS. For each phase, we analyze the simulated elevation-change and ice-velocity, and infer information on the evolving hydrologic drainage system. During the quiescent phase, ice-mass builds up at locations consistent with those observed and water drainage paths become longer with expanding capacity to store subglacial water. These results are attributed to local bedrock topography characterized by large subglacial ridges that act to dam the down-glacier flow of ice and water. In the surge simulation, we model surge evolution through Bering Glacier by implementing a new friction representation that mimics a propagating wave. As the surge progresses through the glacier, drainage efficiency further degrades in the areas of fast-moving ice.

1 Introduction: Glacier Surging, Open Questions and Summary of Approach

The Bering-Bagley Glacier System (BBGS) in southeast Alaska stretches nearly 200 km in length and covers an area greater than 5000 km^2 making it the largest temperate glacier system in the world (B. F. Molnia & Post, 2010a) (see Figure 1). The BBGS is likely the largest surge glacier system outside of the major ice sheets with surge events occurring every 20-25 years (Post, 1972; B. F. Molnia & Post, 2010a; Lingle et al., 1993; B. Molnia & Post, 1995; Herzfeld & Mayer, 1997; Herzfeld, 1998; B. Molnia & Williams, 2001; D. R. Fatland & Lingle, 1998; Mayer & Herzfeld, 2000; B. F. Molnia, 2008; D. R. Fatland & Lingle, 2002; Roush et al., 2003; Fleischer et al., 2010; Josberger et al., 2010; R. A. Shuchman et al., 2010; R. Shuchman & Josberger, 2010). Investigating surging in this massive glacier system is of particular importance when trying to understand heterogeneity in observed glacial dynamics in large and complex systems such as those draining the Greenland Ice Sheet (Jiskoot et al., 2003; Rignot & Kanagaratnam, 2006; Fitzpatrick et al., 2013; Hill et al., 2017; Felikson et al., 2017; Solgaard et al., 2020; King et al., 2020; Choi et al., 2021). Glacier dynamics, especially those of the nonlinear variety such as surging, remain one of the largest sources of uncertainty in estimating future evolution of the ice sheets and their contribution to sea-level rise (Goelzer et al., 2017; Aschwanden et al., 2019; Pörtner et al., 2022).

The most recent surge of the BBGS in 2008-2013 (Herzfeld, McDonald, Stachura, et al., 2013; Burgess et al., 2013; Trantow, 2020) provides a rare opportunity to investigate surging in a large and complex glacier system using modern remote sensing and numerical modeling capabilities. In this paper, we combine recent elevation, velocity and glacier structure (crevasse) data provided by state-of-the art satellite remote sensing missions, together with numerical modeling to better understand how and why the BBGS surges.

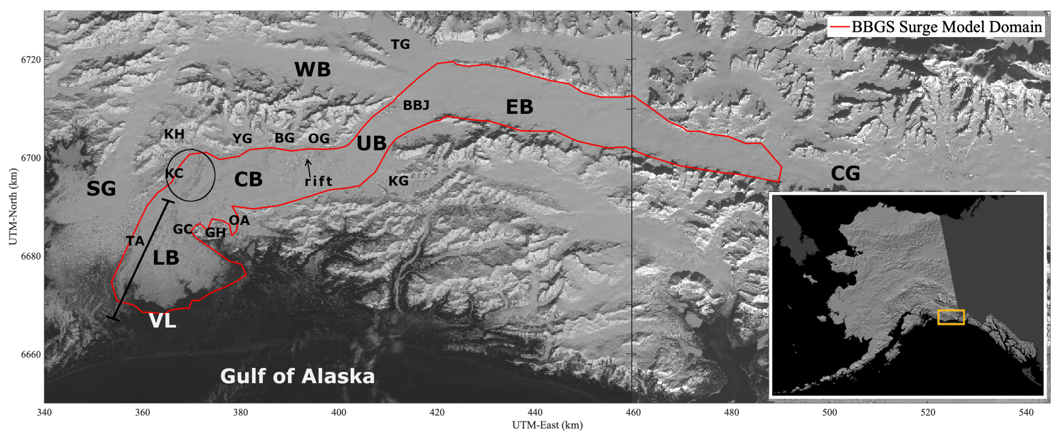

Figure 1. Key features in and around the Bering Bagley Glacier System including the numerical model domain. The red line marks the domain of the BBGS model. LB – Lower Bering Glacier, also referred to as the “lobe area” or the Bering Lobe, CB – Central Bering Glacier; UB – Upper Bering Glacier; EB – Eastern Bagley Ice Field; BBJ – Bering-Bagley Junction; WB – Western Bagley Ice Field; SG – Steller Glacier; CG – Columbus Glacier; VL – Vitus Lake; GH – Grindle Hills; GC – Grindle Corner; KH – Khitrov Hills; TG – Tana Glacier; YG – Yushin Glacier; BG – Betge Glacier; OG – Ovtsyn Glacier; KG – Kuleska Glacier; OA – Overflow Area also known as the Kaliakh Lobe; TA – Tashalish Arm (indicated by black line segment); KC – Khitrov Crevasses (circled in black). The rift is indicated by a black arrow in Upper Bering. The Eastern and the Western Bagley Ice Fields together are also referred to simply as the Bagley Ice Field (BIF). Note the combination of Upper and Central Bering Glacier constitute Bering Glacier’s “trunk” and the imaginary line connecting the Khitrov Hills to the Grindle Hills across Bering Glacier is referred to as Khitrov-Grindle Line. The BBGS is surrounded by the Chugach-Saint Elias mountain range. Background images from Landsat-8 acquired on 28 April 2013 (left) and 7 March 2014 (right). Reference image in lower right: U.S. Geological Survey Map I-2585.

1.1 Glacier surging in the BBGS

In this section, we provide a brief introduction to the phenomenon of glacier surging, especially surging in temperate glaciers in Alaska, with a focus on the BBGS. We define what a surge is and cover the important characteristics of this type of glacier flow, framing open questions with respect to surging in complex glacier systems, and the significance of the work in this paper in contributing to these studies. More comprehensive overviews of glacier surging are given by Jiskoot (2011), and in Chapter 2 of Trantow (2020) as it pertains to the BBGS.

A surge-type glacier system is defined by its quasi-periodic cycle between a long quiescent phase of regular flow speeds and gradual retreat, and a short surge phase when ice flow accelerates 10-100 times its quiescent velocity with ice advancing rapidly down-glacier. There are several types of surge-glaciers, defined by the mechanisms controlling their flow, but in this paper we focus on the type found in Alaskan temperate glaciers, which vary from those found in colder polythermal surge-glaciers, such as those found in Svalbard (Lefauconnier & Hagen, 1991; Dowdeswell et al., 1991; Hambrey & Dowdeswell, 1997; Hamilton & Dowdeswell, 1996; Jiskoot et al., 2000; Murray & Porter, 2001; Woodward et al., 2002; Murray et al., 2003; Hansen, 2003; Nuttall & Hodgkins, 2005; Sund et al., 2009; Mansell et al., 2012; Sund et al., 2014; Flink et al., 2015; Sevestre et al., 2015; Haga et al., 2020; Herzfeld et al., 2022).

In an Alaskan-type surge, the rapid ice-flow acceleration is attributed to an increase in basal water pressure which reduces the friction between ice and the underlying bed structure resulting fast basal motion (Meier & Post, 1969; B. Kamb, 1970; Iken, 1981; W. B. Kamb, 1987). The type of basal motion depends on basal morphology and can consist of basal sliding over "hard" bedrock or bed-deformation in areas with "soft" deformable bed comprised of till (Harrison & Post, 2003).

Internal characteristics determine whether or not a particular glacier is a surge-type glacier, while external climatic effects, including accumulation/ablation (surface mass balance (SMB)) and even weather, are known to effect surge initiation, termination, and the length of each surge-cycle phase for some glaciers (Harrison & Post, 2003). While the present study investigates external forces as it pertains to surging in the BBGS, the main focus will be on the internal dynamics of the system, in particular, the mass transfer of ice and its inferred effect on the basal hydrological system.

1.1.1 Mass transfer

During the quiescent phase, the surface geometry of a surge-type glacier continuously evolves by thickening in some areas and thinning in others. As a result, there is noticeable steepening along the glacier flowline and one can observe "bulges" at the glacier surface when flying overhead (Meier & Post, 1969; W. Kamb et al., 1985; Fowler, 1987; Raymond, 1988; Herzfeld & Mayer, 1997; Herzfeld, 1998), e.g. in altimeter data observations of Bering Glacier in Herzfeld, McDonald, Stachura, et al. (2013). Gradual changes in geometry eventually lead to instability in the system prompting a surge to occur which rapidly redistributes the ice-mass throughout the system resulting in a fractured glacier surface with lower overall slopes (Raymond, 1987). This kind of mass redistribution occurring in a surge-type glacier system leads to definitions of *reservoir areas*, defined as areas of general thickening during the quiescent phase, and *receiving areas* where mass is transferred during the surge phase. A simplified schematic of the mass transfer from a reservoir area to a receiving area during a surge is given in Figure 2.

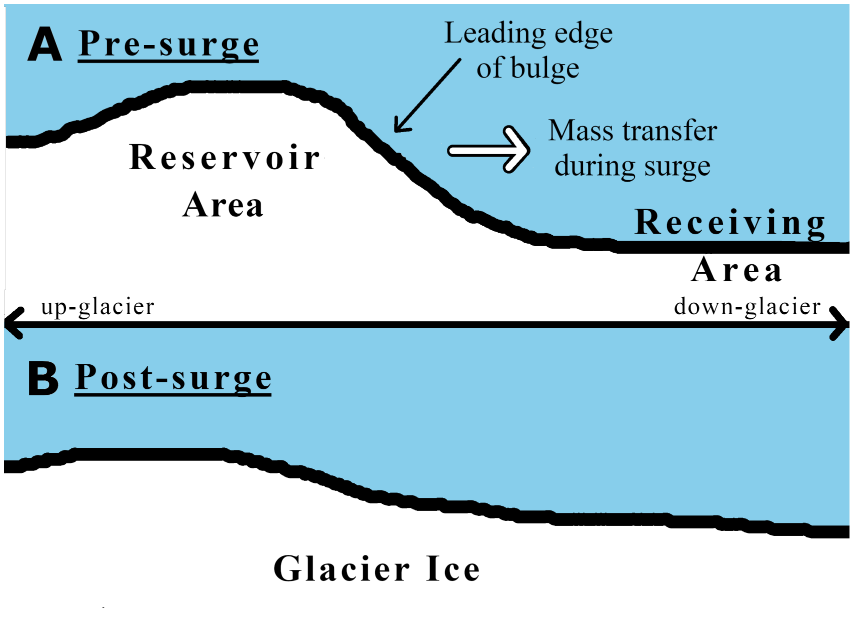

Figure 2. Idealized ice-mass transfer during a surge. The pre-surge profile of an idealized surge glacier is given in subfigure A. The up-glacier reservoir area accumulates ice during quiescence as governed by the internal dynamics of the glacier system (such as bedrock topography). Often, but not always, a surface bulge is observed marking the leading edge of the reservoir area. During a surge, the mass is transferred from the reservoir area to the receiving area down-glacier resulting in a relatively flatter profile as shown in subfigure B. The leading edge of the bulge often coincides with the surge front which propagates as a wave down-glacier during a surge with fast-moving ice in the activation zone up-glacier of the front and un-activated ice moving at quiescent speeds down-glacier of the front.

1.1.2 Hydrologic drainage

A glacier's geometry – i.e., the glacier's thickness, extent and general shape – is tied to local characteristics of the basal hydrological drainage system, but before describing their interaction we introduce the particular forms of a typical Alaskan-type drainage system. During the summer in southeast Alaska, warmer temperatures induce surface melt throughout the glacier system. The meltwater is transferred to the base through englacial tunnels, or moulins, thus requiring the formation of drainage system at the ice/bedrock interface to transfer the water down-glacier (W. Kamb et al., 1985).

During quiescence, it is hypothesized that the glacier possesses a generally efficient drainage system (EDS) comprised of conduits (Lliboutry, 1968), characterized by lower subglacial water pressures relative to the overburden pressure of ice (W. Kamb et al., 1985; Harrison & Post, 2003). Here, the term efficiency refers to the glacier's ability to quickly transfer the input meltwater down-glacier (longitudinally) eventually exiting the system at the terminus.

While the overall efficiency of the drainage system varies throughout the glacier system and throughout the year (Björnsson, 1974; Shoemaker & Leung, 1987; Björnsson, 1998; Boulton et al., 2007; Magnússon et al., 2010), in order for a surge to occur an inefficient drainage system (IDS) must grow and persist long enough to maintain high water pressures to initiate a surge (W. B. Kamb, 1987). An IDS is thought to resemble a linked-cavity system where water pressures can reach overburden pressure causing a decoupling from the bed and fast basal motion (Lliboutry, 1968; W. B. Kamb, 1987). A key difference between the two systems is how they react to an increase in water input to the base. In the IDS case, basal water pressures will rise throughout whereas an EDS will increase its capacity to store the increased meltwater input allowing water pressures to remain level (Lliboutry, 1968; B. de Fleurian et al., 2018).

A changing glacier geometry over quiescence leads to stress conditions that can cause sudden changes in the glacier drainage system (Robin, 1969). An EDS can be destroyed when large overburden pressures from a growing reservoir area overcome the low water pressures experienced by temperate glaciers during the winter season. An IDS then develops up-glacier of the collapse. As melt water input begins to increase in late winter, water pressure increases throughout the IDS which spans the entire width due to restrictive down-glacier drainage (W. Kamb et al., 1985; W. B. Kamb, 1987). If the IDS persists, the rising water pressure will eventually lead to surging, either through a total decoupling of the ice from the hard bed or through dilation of the subglacial sediment (W. B. Kamb, 1987; Truffer et al., 2000; Flowers & Clarke, 2002a, 2002b; B. d. Fleurian et al., 2014). Note that an EDS collapse and an IDS formation may occur without resulting in a surge if the EDS can recover before the water pressure reaches a critical level. The recovery time allowed before surging occurs however, becomes shorter with the growing amount of stored water up-glacier of the EDS collapse. That is, lower effective pressures across the glacier width in these areas are achieved quicker in late-winter/early-spring as the quiescence phase matures.

The persistence of an IDS required for a surge to initiate depends on subglacial and englacial water storage and water storage capacity (Harrison & Post, 2003). The destruction of an EDS traps water that would have normally drained allowing the rapid increase of basal water pressure associated with an IDS. The persistence of an IDS, and its ability to expand to more parts of the glacier system, depends on the amount of stored water available to maintain high basal water pressures. In this paper we show that over the course of quiescence Bering Glacier evolves the capacity to store more and more subglacial water through the development of hydropotential wells and longer, more-transverse drainage paths, thus challenging the concept of a binary EDS/IDS classification described above. We also investigate the progression of the surge as it relates to expanding drainage inefficiencies throughout the actively surging region. Our investigation of changes of the subglacial hydrology of the glacier during surge evolution does not require explicit modeling of the hydrological system, and instead we analyze hydropotential as an indicator (Shreve, 1972).

Stored water during a surge is reflected by the occurrence of large outburst floods at the glacier terminus, which is accompanied by surge termination and a return to normal flow, lower water pressures and an EDS (Humphrey & Raymond, 1994; Harrison & Post, 2003). Such outburst floods have been observed for previous surges of the BBGS (D. R. Fatland & Lingle, 1998). The current study uses remote sensing data to demonstrate a return to efficient drainage after the surge where the BBGS has less capacity to store subglacial water.

1.1.3 A surge kinematic wave

Returning to the picture of mass transfer, during a surge, a surface bulge initiating at the edge of a reservoir area will propagate down-glacier as a kinematic wave coinciding with a surge "front" (W. Kamb et al., 1985). We refer to this process as *surge wave propagation*, which is triggered at some initiation location. As the surge front propagates down-glacier, the increased driving stress changes the basal hydrological characteristics beneath it, causing drainage inefficiencies (Fowler, 1987). These efficiency-destroying hydrologic changes lead to increased water pressure, reduced friction and thus increased basal motion, which accounts for nearly all the accelerated flow speeds during a surge

(Harrison & Post, 2003; Cuffey & Paterson, 2010). Therefore, as the surge wave moves down-glacier, it activates increased basal motion for a section of the glacier up-glacier of the surge front (Fowler, 1987), leading to accelerating (surging) ice within an "activation zone".

Studies on smaller surge-glaciers find that the entire glacier can be actively surging simultaneously once the surge wave reaches the terminus, e.g. Finsterwalderbreen in Robin and Weertman (1973) whose length is ≈ 14 km. Turrin et al. (2013) maps the kinematic wave for the latest BBGS surge and suggest that the activated portion of the glacier extends up to the Bering-Bagley Junction (BBJ), near their proposed surge-trigger area. surge wave effects are also felt up-glacier of the activation zone, given by observed en-échelon crevasses in the Bagley Ice Field for the last two surges (Herzfeld & Mayer, 1997; Herzfeld et al., 2004; Herzfeld, McDonald, Stachura, et al., 2013).

1.1.4 What constitutes a surge?

Smaller-scale acceleration events, lasting on the order of a single day, are known to occur during the quiescent phase of some surge-glaciers and lead to temporary relaxation of the increased driving force that accompanies surface steepening (Meier & Post, 1969; B. Kamb & Engelhardt, 1987; Raymond, 1987; Harrison & Post, 2003). Often termed "mini-surges", these pulses of increased flow are sometimes premonitory to a glacier surge (B. Kamb & Engelhardt, 1987). In some cases, the mini-surge events are tied to the sudden release of subglacial water storage (Jansson et al., 2003), which we investigate in the current study for the BBGS where mini-surges have been observed (B. F. Molnia & Post, 2010b; Burgess et al., 2013).

During the true surge phase, which has prolonged acceleration on the scale of months to years, a rapid and full-scale acceleration event redistributes ice throughout the entire glacier system resulting in drastic elevation changes, with rapid thinning of the former reservoir areas, thickening in the receiving areas and drawdowns along the margins of the glacier (Meier & Post, 1969; Raymond, 1987; Harrison & Post, 2003; Fowler, 1987, 1989). Heavy and wide-spread crevassing also occurs during the surge phase, indicative of rapid deformation, horizontal and vertical displacement of ice and sudden changes in flow speeds. In Trantow and Herzfeld (2018), we used measurements of surge-crevasses to estimate model parameters during the early-2011 surge phase of the BBGS (March-April 2011). We utilize and build upon this parameterization in the current study when modeling the BBGS's surge phase.

The exact length and timing of the surge phase can be unclear in a complex glacier system such as the BBGS. Most studies on surges are conducted on smaller glaciers that consist of a single reservoir area in the accumulation zone and a single receiving area down-glacier near the terminus, e.g., Variegated Glacier, Alaska (W. Kamb et al., 1985; Eisen et al., 2005; Jay-Allemand et al., 2011a) or Black Rapids Glacier, Alaska (Raymond et al., 1995; Heinrichs et al., 1996; D. Fatland et al., 2003). However, as we show in this study, a large and complex glacier system like the BBGS can consist of multiple reservoir and receiving areas which can lead to a complicated picture of the surge evolution. Moreover, a complex glacier system can have both surge-type and non-surge-type parts, with different processes, such as surge initiation and re-initiation, occurring in different locations and at different times (Herzfeld, 1998; Herzfeld, McDonald, Stachura, et al., 2013). The BBGS shares this property of complexity with sections of the Greenland and Antarctic ice sheet margins, where surge-type glaciers are found neighboring non-surge-type glaciers and accelerating outlet glaciers (Jiskoot, 1999; Herzfeld, 2004; Sevestre et al., 2015). Thus, the study of the BBGS surge provides extra layers of insight into the complex glacier acceleration found along the ice sheet margins, compared to the more commonly studied surges of smaller mountain glaciers.

1.2 Observations of the BBGS surge in 2008-2013

Observations and analyses of the Bering-Bagley Glacier System and its surges before 2008 are summarized in (B. F. Molnia & Post, 2010b). For the most recent BBGS surge however, peak surge activity occurred in early 2011 affecting mostly Lower and Central Bering Glacier (Figure 3) (Herzfeld, McDonald, Stachura, et al., 2013; Trantow & Herzfeld, 2018), while lesser surge activity was observed in Bering Glacier's trunk where elevated ice-velocities were observed in 2008 (Herzfeld, McDonald, Stachura, et al., 2013; Burgess et al., 2013). Surge activity continued to affect parts of the BBGS until 2013 (Herzfeld, McDonald, Stachura, et al., 2013; Trantow, 2020), and we therefore refer to the total surge phase as lasting from 2008 to 2013 despite limited observed surge activity between 2009 and 2010 (Burgess et al., 2013). Henceforth, we refer to the surge activity from 2008-2010 as the first, or initial surge phase, while the surge activity in 2011-2013 is referred to as the second, or major, surge phase as the most wide-spread dynamical activity occurred during this time (Herzfeld, McDonald, Stachura, et al., 2013). We expand on these observations in the following.

1.2.1 First (initial) surge phase

Mean surface speeds in late 2007 and early 2008 were at quiescent levels ($\leq$1 m/day, 365 m/a) in the Bagley Ice Field and Upper Bering Glacier (LeBlanc, 2009). Around this time, the first sign of surge activity came after the opening of a large longitudinal rift (Figure 3(a-b)). This rift, also observed during the 1993-1995 surge (Herzfeld, 1998), reached 60 m in depth upon forming and grew in size throughout the surge reaching nearly 200 m in width and 10 km in length by 2013 (Herzfeld, McDonald, Stachura, et al., 2013; Trantow, 2020).

Between September 2008 and February 2009 surface speeds increased in Upper and Central Bering, while quiescent speeds remained in Lower Bering below the Khitrov-Grindle line (Turrin et al., 2013; Burgess et al., 2013). The maximum observed velocity was 7 m/day (2555 m/a) in Central Bering but peak speeds might have been even higher (Burgess et al., 2013). By early 2010, surface speeds in Central Bering returned to their peak quiescent values while velocities in the lower Bagley Ice Field and Upper Bering remained slightly elevated above quiescent speeds at 2 m/day (720 m/a) through 2010.

1.2.2 Second (major) surge phase

In early 2011, Bering Glacier's dynamics changed to a full-scale surge resulting in crevassing throughout a large portion of the glacier (Herzfeld, McDonald, Stachura, et al., 2013). A reservoir area in the lower-Central Bering, observed by (Herzfeld, McDonald, Stachura, et al., 2013) and (Burgess et al., 2013), transferred its mass down-glacier along the northern branch of the flow regime to the lower Tashalish Arm area (the westernmost part of the Bering lobe, Figure 3(c)). The former reservoir area experienced surface lowering of 40-70 meters while the receiving area gained 20-40 meters of surface elevation by fall 2011 (Herzfeld, McDonald, Stachura, et al., 2013). The bulge collapse resulted in the formation of large surge crevasses in the Khitrov crevasse field (Figure 3(d)). The thickening continued to move downstream until it reached the terminus, extending 2-4 km further into Vitus Lake (Turrin et al., 2013).

While very few measurements of velocity in 2011 were reported in Burgess et al. (2013), one 11-day interval in the beginning of July shows a peak velocity of 9 m/day (3285 m/a) near the boundary of Upper and Central Bering. Burgess et al. (2013) provided no velocity measurements in Lower Bering for 2011, nor any additional estimates beyond July 2011. Velocity measurements of Lower Bering from Trantow and Herzfeld (2018) show surge velocities between March and April 2011 reaching at least 21 m/day.

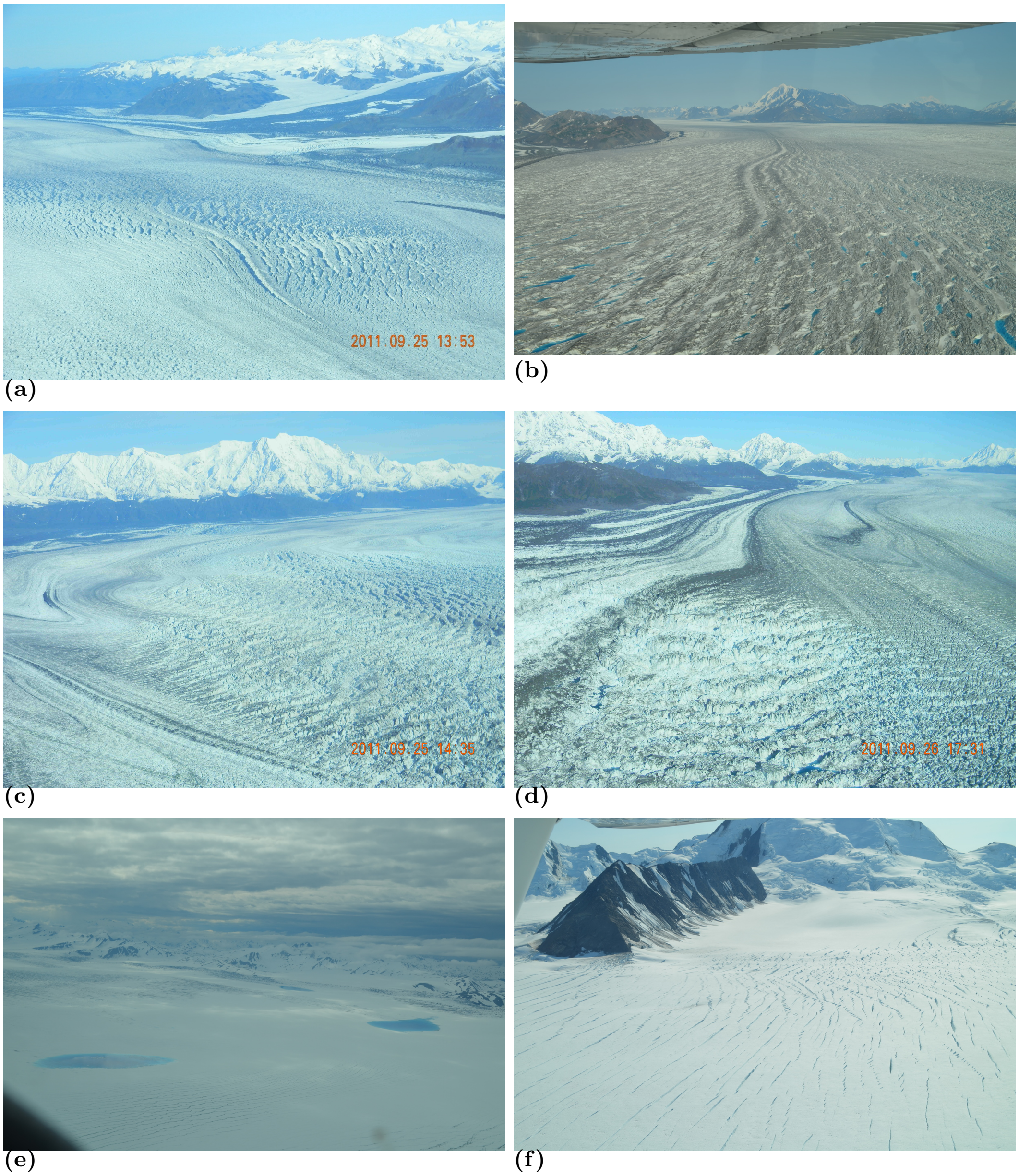

Figure 3. Imagery from the airborne campaign flights over Bering Glacier 2011-2013 (Herzfeld, McDonald, Stachura, et al., 2013). The large longitudinal rift in Upper Bering Glacier along the northern branch in (a) September 2011(looking down-glacier from the northeast) and (b) in August 2013 with water in the surrounding crevasse field (looking up-glacier). (c) Surge-induce crevasses in Upper Tashalish Arm (September 2011). (d) A former reservoir area within the Khitrov crevasse field (foreground) during the second stage of the surge in early 2011 (September 2011). (e) Three supraglacial lakes in Central Bering Glacier, present only in the second surge phase, as observed in July 2012. (f) En-échelon crevasses along the southern margin of the Bagley Ice Field (August 2013) indicating surge effects being felt far up-glacier of the acceleration in Bering Glacier.

Aerial observations from the campaigns of Herzfeld, McDonald, Stachura, et al. (2013) revealed that the surge continued to induce significant effects throughout the glacier system in 2012 and 2013. The presence of large supraglacial lakes in the summer of 2012 in Central Bering (Figure 3(e)) indicated that the glacier remained in a state of inefficient drainage with the clear, glacier-blue surface meltwater being unable to drain to the glacier bed after the destruction of the quiescent-phase drainage system. By 2013 most of the dynamical activity in Bering Glacier had ceased, though the effects of the surge were still being felt in the Bagley Ice Field as demonstrated by the opening of fresh en-échelon crevasses (Figure 3(f)). These characteristic en-échelon crevasses form when the kinematic energy from the surge causes deformation at pre-existing weaknesses in the ice caused by the local topography (Herzfeld & Mayer, 1997; Herzfeld et al., 2004). A more comprehensive documentation of observations from the latest surge is given in Chapter 2 of Trantow (2020).

1.3 Approach Overview and Limitations

The present study investigates a surge cycle of the BBGS using numerical modeling together with satellite and airborne observations. It broadens our understanding of surging by using the BBGS, a large and complex glacier system, as a case study rather than a smaller glacier, such as Variegated Glacier, from which most of our knowledge on (Alaskan-type) surging has been derived. Traditional remote sensing methods used to study glacier dynamics are complicated by the nonlinear movement of surge glaciers, and comprehensive in-situ measurements are impossible on the BBGS due to its immense size and remoteness. Therefore the observational aspect of our approach combines a broad range airborne and satellite data in novel ways, as described in Section 2, to quantify and describe the BBGS surge cycle. We utilize both previous and new estimates of surface and bed topography, velocity and crevasses, and derive second-order products such as hydropotential maps which are used to estimate water drainage paths despite an absence of subglacial hydrological measurements for the BBGS.

Our observations also inform and constrain a full-Stokes, transient numerical model that simulates the phases of the BBGS surge cycle. Numerical modeling provides insight into the physical mechanics that govern surging and glacial acceleration, a key uncertainty in global sea-level rise estimates. The main difficulty in modeling glacial acceleration is the nonlinear nature of the dynamics in both time and space. Capturing dynamically complex ice movement requires high spatiotemporal resolution in the model to allow rapidly evolving parameterization. Moreover, because there is significant basal motion during a surge, as well as a relatively large depth-to-width ratio for the BBGS, the computationally-expensive full-Stokes implementation of ice flow (see Section 3.2) is required to adequately model the observed flow behavior (Gudmundsson, 2003; Hindmarsh, 2004; Le Meur et al., 2004; Trantow, 2014), rather than a more computationally efficient representation such as the Shallow Ice Approximation (SIA, Hutter (2017)). Finally, since high temporal resolution is necessary, even during quiescence where significant changes can occur on the order of days, a large amount of time steps are required to simulate the entire 20-25 year surge cycle.

All modeling experiments are carried out on a desktop computer (iMac 3.6GHz 8-core i9 processor with 64 GB of RAM), where the run time for the completion of single simulation can last up to several weeks. Because of the significant computational time, we are unable to run large ensembles of model simulations with various combinations of modeling parameters to identify ideal parameterization. We therefore base our parameter values on the diagnostic runs derived in Trantow and Herzfeld (2018) for the surge experiments and (Trantow, 2014) for the quiescent experiments. For the current study, we simulate only the initial phase of the surge to demonstrate our approach for modeling surge progression in the BBGS and use data products derived from satellite observations (CryoSat-2, Sentinel-1 and Landsat-8) to investigate the second phase of the recent surge.

While limited by the amount of simulations we can realistically run, the experiments we discuss in this study still provide valuable insight into how and why the BBGS surges. The model physics, along with our experimental designs concerning the modeling of the quiescent and surge phases of the BBGS, are covered in Section 3.

After the data and modeling methods are introduced, we present the results of the quiescent phase in Section 4 and the initial surge phase in Section 5. For each phase, we investigate (1) the mass redistribution and geometrical changes in the glacier system, (2) the hydrologic implications of those changes, and (3) how these results can improve our model representations. In addition, though not explicitly modeled, we propose methods for initiating a surge in Section 5.1 while in Sections 5.3 and 5.4 we utilize CryoSat-2 observations in the absence of modeling, to investigate hydropotential in the second phase of the glacier system from 2011-2013 and the return to quiescence.

2 Data and Observations

2.1 Surface and Bedrock Digital Elevation Maps (DEMs)

This study utilizes data products derived from satellite remote sensing data, together with airborne observations from the 2011-2013 campaigns of Herzfeld, McDonald, Stachura, et al. (2013). The mass redistributions throughout the surge-cycle are quantified through measurements and simulations of surface elevation and elevation-change. The radar altimeter measurements provided by the European Space Agency's (ESA's) CryoSat-2 satellite (Wingham et al., 2006) provide height estimates of the glacier surface at sufficient spatiotemporal resolution so as to generate elevation maps of the BBGS every six months at 200 m-by-200 m resolution (Trantow & Herzfeld, 2016). We utilize such maps in the current study to initialize and constrain model simulations and compare the elevation-change results to those quantified in Trantow and Herzfeld (2016). While Trantow and Herzfeld (2016) created six Digital Elevation Models (DEMs) for the summer and winter seasons between 2010/2011 and 2013, for the current analysis we also derive a Summer (May-October) 2016 DEM of the BBGS to represent the glacier surface in the early quiescent phase (Figure 4(a)), and to initialize the quiescent phase simulations presented in Section 4.

More specifically, the Summer 2016 ice-surface data is attained from a CryoSat-2 processing (retracking) technique that combines swath-processing with the Threshold First Maximum Retracking Algorithm (TFMRA) (Helm et al., 2014). Swath-processing provides over 150 times more height estimates than traditional retracking methods, and provides the best DEM available for numerical modeling (Trantow et al., 2020). The TFMRA-swath data is based on the Baseline-C version of the CryoSat-2 L1B data (Bouffard, 2015), as this was the latest data version at the time of analysis.

We apply a filter to the Summer 2016 data that is specifically designed to eliminate outliers in CryoSat-2 datasets through utilization of computed variograms. Next, we use the Advanced Kriging method to derive a 200 m resolution DEM of the entire BBGS surface. This data processing pipeline is laid out fully in Trantow and Herzfeld (2016), while Herzfeld et al. (1993) introduces the method of Advanced Kriging which builds upon the Ordinary Kriging method to better interpolate elevations on a glacier surface, particularly one that is highly-crevassed. Furthermore, the influence of CryoSat-2 data processing techniques on elevation analysis and numerical modeling results is covered in Trantow et al. (2020).

The Summer 2016 ice-surface topography initializes the quiescent phase experiments because it corresponds to the post-surge/early-quiescent phase geometry after the most recent surge. Initial ice-surface topography for the surge phase experiments are given by

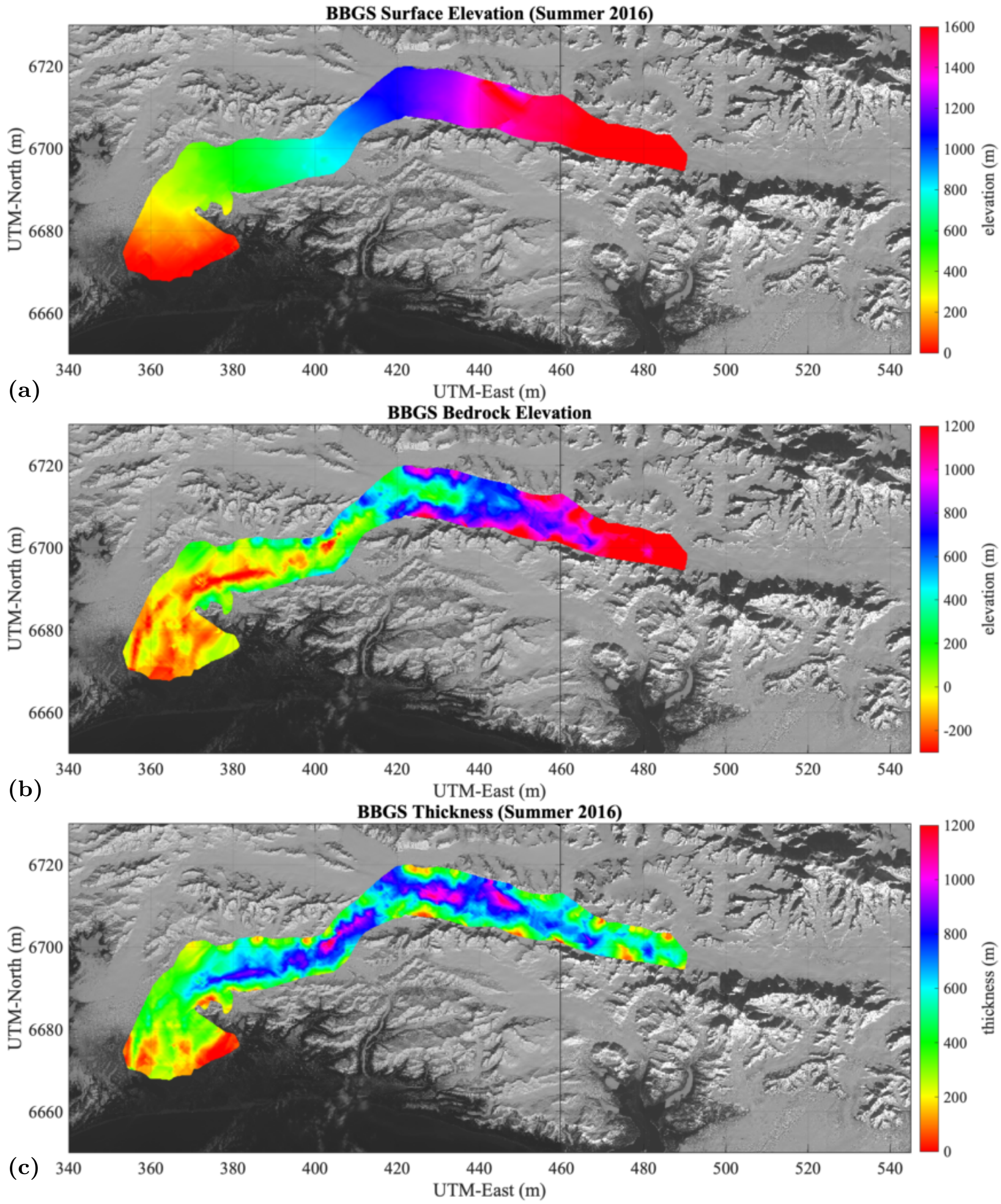

Figure 4. BBGS geometric data sets for early quiescence. (a) Surface DEM derived from CryoSat-2 measurements from May 2016 to October 2016 (Summer 2016), which represents surface topography in early quiescence and is used to initialize quiescent phase experiments. (b) Bed DEM derived from the JPL WISE ice-penetrating radar campaign in 2012, which is fixed for all BBGS simulations. (c) Glacier ice-thickness for Summer 2016 derived from subtracting the bed elevation in (b) from the surface elevation in (a). The resolution of each data product in the figure is 200 m-by-200 m.

the final state of the quiescent simulation (end-of-quiescence surface topography, see Section 5.2).

The input basal bedrock topography (Figure 4(b)), common to all our BBGS simulations, is derived from ice-penetrating radar measurements provided by the Warm-Ice

Sounding Explorer (WISE) acquired during a 2012 campaign to the BBGS by NASA's Jet Propulsion Laboratory (Rignot et al., 2013). Derivation of this 200 m-by-200 m bedrock topography DEM of the BBGS is described in Trantow and Herzfeld (2018), while additional bedrock representations for the BBGS are discussed in Chapter 4.1 of Trantow (2020).

2.2 Velocity Maps

In this study, we utilize velocity estimates from the latest BBGS surge phase and most recent quiescent phase to get a full picture of surface velocity throughout the surge cycle. Velocity estimates before and during the initial phase of the latest surge are given by Turrin et al. (2013) ($\approx$1 km resolution) and Burgess et al. (2013) ($\approx$ 200 m to 700 m resolution). We do not have the explicit velocity data from these last two studies and instead rely on the maps presented in the respective papers.

For the major surge phase, we utilize the sparse velocity estimates in Lower Bering in early-2011 provided by Trantow and Herzfeld (2018), and a more complete velocity map of the BBGS toward the end of the surge in 2013 originally given in Trantow (2020). These last two velocity estimates are given at 75 m-by-75 m resolution and are derived using feature tracking methods applied to Landsat-7 (Goward et al., 2001) and Landsat-8 imagery (Roy et al., 2014) respectively. Feature tracking on Landsat imagery is performed using the Image georectification and feature tracking toolbox (ImGRAFT) (Messerli & Grinsted, 2015).

A quiescent phase map at 300 m-by-300 m resolution is also derived in Trantow (2020) using feature tracking methods applied to Sentinel-1 SAR imagery (Geudtner et al., 2014; Veci et al., 2014; Trantow, 2020). Sentinel-1 imagery typically provides more frequent and complete velocity maps compared to Landsat imagery due to shorter temporal baselines provided by the Sentinel-1 satellite tandem, larger spatial coverage per image, and the fact that SAR imagery are not obstructed by cloud cover.

The observationally-derived Summer 2016 velocity map is given along-side the modeled quiescent-phase velocity in Section 4.4 to allow better visual comparisons. Similarly, the major surge phase velocity maps originally derived in Trantow and Herzfeld (2018) and Trantow (2020) are provided Section 5.3 alongside additional observationally-derived data products.

We note here that attaining accurate and comprehensive velocity measurements through feature-tracking methods, as used in each estimate listed above, are made extremely difficult by surge activity due to the large-scale and nonlinear changes (D. R. Fatland & Lingle, 1998; Trantow & Herzfeld, 2018). The lack of reliable velocity estimates complicates traditional glaciology approaches to investigate glacier dynamics, therefore driving the need to incorporate additional data-types, such as crevasses (Trantow & Herzfeld, 2018), to better understand a BBGS surge. In the current analysis, we utilize the crevasse-based insights gained in Trantow and Herzfeld (2018) with regards to parameterizations of the BBGS model during the early-2011 part of the surge, to derive a spatiotemporally-variable friction representation to represent a surge wave passing through Bering Glacier in the surge phase simulations (Section 3.3.2.2). The surge wave implementation also relies on the velocity estimates of Turrin et al. (2013) who track a kinematic wave progressing through the BBGS.

2.3 Airborne Imagery

Four airborne campaigns were conducted by the authors and their research group in Fall 2011, Summer 2012, Fall 2012 and Fall 2013 to document the BBGS surge using a sub-meter resolution laser profiler, imagery from handheld cameras and nadir-pointing video (Herzfeld, McDonald, Stachura, et al., 2013; Herzfeld, McDonald, & Weltman, 2013). While Trantow and Herzfeld (2018) utilized the airborne laser altimeter data to gain crevasse-based insights on the early-2011 part of the recent surge, the current study only utilizes the airborne imagery collected during these campaigns in order to provide visual references to BBGS surge features described in the text (Figure 3).

2.4 Surface Mass Balance

For purposes of modeling the long quiescent phase, we incorporate estimates of surface mass balance for the BBGS, which require a synthesis of several studies due to discrepancies in estimates. Annual accumulation and ablation estimations for the BBGS are given by Tangborn (2013) as a function of ice-surface elevation while Larsen et al. (2015) provide SMB rates for glaciers across Alaska, including the BBGS. Tangborn (2013) employs a precipitation-temperature-area-altitude (PTAA) model using daily precipitation and temperature observations from nearby weather stations to derive historical net ablation and accumulation balances with respect to ice-surface altitude from 1951-2011. More recently, Larsen et al. (2015) used airborne altimetry to estimate regional mass balances for Alaskan mountain glaciers. The rates given by Tangborn (2013) estimate much higher melt-rates for the BBGS which are at odds with the more recent and comprehensive measurements by Larsen et al. (2015). Our numerical model therefore enforces accumulation and ablation rates whose magnitudes better reflect those measured by Larsen et al. (2015), but still employs the quasi-linear relationship of SMB rates with respect to ice-surface altitude derived by Tangborn (2013).

Figure 5 shows the linear relation between the model's enforced SMB and ice-surface elevation. The slope of the line is derived from a linear approximation, fit in a least-squares sense, of the mean net mass balance for the BBGS from 1951-2011 converted to meters per year of ice from the original mean-water-equivalent per year in Tangborn (2013). This conversion requires an assumption of constant ice density which is set at 917 kg/m^3 (ice density for the 0°C isothermal assumption). The y-intercept is adjusted so that the function spans the observed range given by Larsen et al. (2015). A histogram describing the distribution of ice-surface elevation at each model surface-node throughout the BBGS is also shown in the same plot.

Importantly, we do not model firn compaction or ice-density variation at the glacier surface in general (see e.g. Huss (2013)). Instead, we are assuming that the SMB adds mass to the system in the form of fully compacted glacier ice at 917 kg/m^3 ice density. Therefore, while the input and output of total mass is consistent with observations, the exact form of that mass differs in our model. We return briefly to this discussion on Section 4.1 when bounding mass loss estimates given by our model.

The mathematical equation for annual mean-SMB (in terms of meters of ice gain/loss), smb_{mean}, that the model uses is given by glacier surface elevation z_s:

$$smb_{mean} = \Big(0.0015 \cdot z_s - 2\Big)/0.917 \tag{1}$$

This SMB equation for the BBGS places the equilibrium line altitude (ELA) at 1333 ft, above which the glacier experiences net accumulation and below which experience net ablation. This places most of the Bagley Ice Field in the accumulation zone and all of Bering Glacier in the ablation zone during the time of the latest surge (Trantow & Herzfeld, 2018).

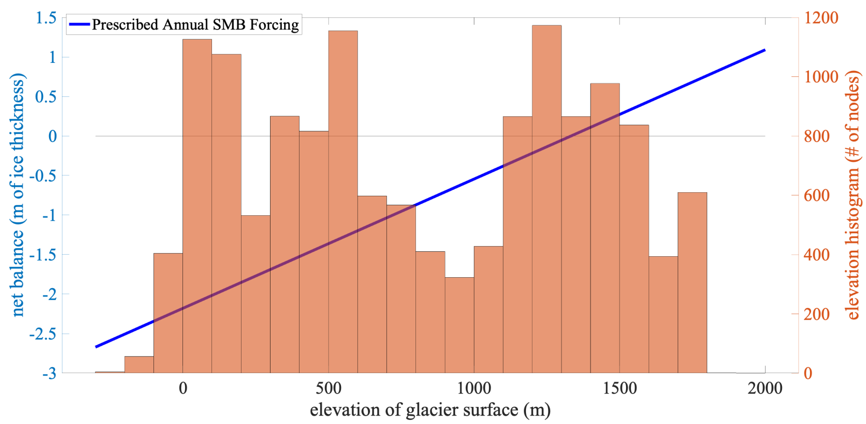

Figure 5. Annual net surface mass balance estimates for Bering Glacier as a function of elevation derived from Larsen et al. (2015) and Tangborn (2013). The blue line gives the linear approximation of the relationship between glacier surface elevation and surface mass balance based on Tangborn (2013) while the magnitude of surface mass balance is based on Larsen et al. (2015). The histogram in red shows the distribution of model surface-nodes throughout the BBGS within 100 m elevation bins based on the beginning-of-quiescent state of the glacier (Summer 2016 geometry, see Section 3.3.1).

3 Numerical Model

3.1 Modeling Approach

The BBGS model was built using the finite element software Elmer/Ice (Gagliardini et al., 2013) and has been used in previous diagnostic studies that used a crevasse-based approach to constrain unknown model parameters during the early-2011 portion of the latest BBGS surge (Trantow & Herzfeld, 2018). Our previous work focused on synthesizing the model-data connection using a variety of high-quality data inputs, which includes observations of surface height (Trantow & Herzfeld, 2016), velocity, crevasse location and crevasse orientation (Trantow & Herzfeld, 2018), and showed that model results and parameter optimization were robust to relative uncertainties in the observational inputs (Trantow et al., 2020). In the current study, we switch to prognostic modeling by performing longer transient simulations of both the quiescent phase (20 years, 10-day time steps) and the initial surge phase (≈2 years, 5-day time steps), while utilizing the insight with regards to model parameterization and model-data connection derived in our previous studies. These modeling results are supplemented with both new and existing observational analysis, and together our model-data analyses, provide a full picture of an entire surge cycle of the BBGS regarding dynamics, ice-mass evolution and implications on water drainage paths.

The model uses a full-Stokes representation, together with a Glen rheology, to model ice flow (Section 3.2). Full-Stokes is necessary to adopt due to the significant amount of basal motion during a surge (Hindmarsh, 2004; Cuffey & Paterson, 2010). Moreover, the extreme crevassing and vertical displacement of ice occurring during a surge, particularly in the BBGS (Herzfeld, 1998), does not allow any simplifying assumptions to the stress tensor common to full-Stokes approximations such as the SIA. The full-Stokes representation also allows the ice model to capture the effect of spatial variability in the bedrock geometry (Gudmundsson, 2003), which is significant for the BBGS (Trantow & Herzfeld, 2018). Our approach will therefore allow our relatively high quality bedrock and ice-surface topography inputs (200 m resolution) to explain as much of the spatial variability in the glacier's observed dynamics as possible, with model resolution set at a similar horizontal scale (400 m element length resolution).

The boundary conditions of the modeled glacier with respect to the atmosphere, underlying bedrock and mountainsides are covered in Section 3.3. While overlying atmospheric pressure is negligible, mass accumulation and ablation at the glacier surface is prescribed in this model and is particularly important for the longer quiescent phase runs (Section 3.3.1).

Perhaps the most important aspect of our ice-flow model is the treatment of the ice-bed boundary, in particular, the prescribed friction representation which describes basal motion in the ice dynamics (Section 3.3.2). We do not consider bed composition in our simulations (hard vs. soft bed representation) and instead simply model the effect of changing friction at the ice-bed interface. Following Harrison and Post (2003), we use the term "basal motion" to represent the various processes under the ice that result in non-zero basal velocities. Basal motion accounts for nearly all the dynamics during a surge with internal deformation (creep flow) contributing very little to the observed ice-velocities (Cuffey & Paterson, 2010). Even in the quiescent phase of the BBGS, significant basal motion is required to capture the observed velocities throughout most of quiescence (Trantow, 2014, 2020).

The prescribed friction representation differs in the quiescent and surge phase experiments, though both utilize a linear relationship between velocity and shear stress at the glacier base due to its surprising capability to capture observed dynamics when coupled with accurate and high-resolution topography inputs as shown in previous studies (Trantow, 2014; Trantow & Herzfeld, 2018). The quiescent phase uses a uniform basal friction representation explicitly, while in the surge phase parameterization of the linear friction relationship is allowed to spatiotemporally evolve reflecting a passing surge wave (Section 3.3.2.2). We only simulate the early surge phase in this study, mostly due to the computational limitations covered in Section 1.3, however, the results motivate the use of this type of friction representation to simulate the entire surge phase in future studies that have better computational resources.

Our first goal in modeling for each phase is to analyze mass redistribution within the glacier system, that is, identify reservoir and receiving areas and estimate elevation-change which we can compare to observations. Second, we want to use the simulated mass transfer to estimate changes in hydrological drainage characteristics, which are known to play a major role in flow behavior and state switching in a surge-type glacier. Importantly, we do not explicitly model the subglacial hydrological system and instead attempt to infer local drainage pathways based on the changes in ice thickness and surface slope, and its relationship with the local bedrock topography. We do this by calculating the hydropotential, or the Shreve potential (Shreve, 1972), throughout the surge cycle, which is described and further motivated in Section 3.4. Explicit modeling of water flow in glaciers has become more sophisticated and better understood in recent years, as detailed in Flowers (2015), however there remains difficulty in applying these advances to real, complex glacier geometries (Flowers, 2015), such as the BBGS (Trantow, 2014). We therefore focus on attaining realistic simulations of mass transfer during the surge cycle as our main goal and make use of its hydrological implications, and we save implementation of a coupled ice-dynamic and hydrological model for future work.

In this study, we simulate the quiescent phase (Section 4) and initial surge phase (Section 5) separately as the model is not yet advanced enough to inherently model transition between flow states, that is, triggers causing surge initiation and surge cessation. There are single unified friction laws, such as the Schoof-Gagliardini Law (Gagliardini et al., 2007), that have the ability to model the state-switching behavior in surge glaciers. However, the inherent complexity of the Schoof-Gagliardini Law makes it difficult to accurately parameterize and achieve numerical stability as shown in Trantow (2014) for the BBGS. While the ultimate goal of our BBGS surge model is to incorporate such a unified friction law, for this study we will instead propose surge initiation criteria based on the end-of-quiescent state of the glacier given by the resulting quiescent runs (Section 5.1). Since we do not model the full surge phase in our experiments here, we use utilize satellite observations from 2011 and 2013 to investigate the second surge phase (Section 5.3) and the end-of surge state where we postulate possible surge arrest criteria (Section 5.4).

Finally, our modeling approach does not include seasonal variability but instead looks at inter-annual (secular) trends. In particular, we enforce an observed mean annual surface mass balance (SMB) uniformly throughout the entire model duration. While seasonal changes in glacial water are known to play a role in the intra-annual timing of surges (Raymond, 1987), our analysis will focus on inter-annual and seasonally-independent changes in hydrological characteristics of the subglacial drainage system, which govern the approximate length of the surge cycle phases. That is, we focus on modeling dynamics resulting from internal characteristics of the glacier system, which are known to determine whether a glacier is or is not a surge-type glacier. If surging depended strongly on seasonal components such as precipitation, then we would expect neighboring glaciers to have similar dynamic responses as those observed for the BBGS. For example, the neighboring Steller Glacier (see Figure 1) is not known to surge. In fact, Trantow (2020) has shown that local precipitation and temperature anomalies have no correlation with the timing and duration of the last three BBGS surges. We proceed now to introduce the model particulars in more depth.

3.2 Flow Law for Temperate Ice

The full-Stokes equations utilize conservation laws to describe the flow of ice via internal deformation as forced by gravity. Stokes flow simplifies the more general Navier-Stokes equations for viscous fluid flow by assuming the inertial forces are negligible in comparison to viscous forces. Momentum conservation is given by

$$\nabla \cdot \boldsymbol{\sigma} + \rho \boldsymbol{g} \equiv \nabla \cdot (\boldsymbol{\tau} - p\boldsymbol{I}) + \rho \boldsymbol{g} = 0, \tag{2}$$

and conservation of mass is given by

$$\nabla \cdot \boldsymbol{u} = tr(\dot{\boldsymbol{\epsilon}}) = 0, \tag{3}$$

where $\boldsymbol{\sigma} = \boldsymbol{\tau} - p\boldsymbol{I}$ is the Cauchy stress tensor, $\boldsymbol{\tau}$ the deviatoric stress tensor, p the pressure, ρ the ice density, $\boldsymbol{g} = (0, 0, -9.81)$ the gravity vector, $\boldsymbol{u}$ the velocity vector and $\dot{\boldsymbol{\epsilon}} = \frac{1}{2}(\nabla \boldsymbol{u} + (\nabla \boldsymbol{u})^T)$ the strain-rate tensor.

The relation between stress and the internal flow of ice is given by Glen's Flow Law (Glen, 1955),

$$\boldsymbol{\tau} = 2\eta \dot{\boldsymbol{\epsilon}}, \tag{4}$$

where η is the effective viscosity defined as,

$$\eta = \frac{1}{2} A^{-1/n} \dot{\epsilon}_e^{(1-n)/n}, \tag{5}$$

where $\dot{\epsilon}_e$ is the effective strain-rate and n the Glen exponent, set as $n = 3$ for all experiments in this study, which is a well established value for temperate glacier flow (Hooke, 1981; Greve & Blatter, 2009; Cuffey & Paterson, 2010). The rate-factor $A = A(T')$, a rheological parameter that depends on the ice temperature via an Arrhenius law, is given by

$$A(T') = A_0 exp(\frac{-Q}{RT}), \tag{6}$$

where Q is the activation energy, R the universal gas constant, A_0 a pre-exponential constant, and T' the temperature relative to the pressure melting point. The BBGS is a temperate glacier, implying the temperature of most of the ice is at or near the pressure melting point throughout the entire year. Therefore, we employ an isothermal assumption with ice temperature set to 0°C resulting in a rate-factor of $A(0°C) = 75.7MPa^{-3}a^{-1}$. Equations 2-3.2 describe the creep deformation of glacier ice under gravitational stress. Recall, however, that basal motion constitutes the majority of the the glacier movement during a surge, and dominates movement in the BBGS quiescent phase dynamics as well (Trantow, 2014), and therefore creep motion is expected to contribute relatively little to the overall dynamics in the BBGS surge cycle.

3.3 Boundary Conditions

3.3.1 Ice-Atmosphere Boundary and Surface Mass Balance Forcing

At the surface of the glacier, a stress-free boundary condition is employed

$$\boldsymbol{\sigma n_s} = -p_{atm}\boldsymbol{\sigma} \approx 0 \tag{7}$$

which assumes the atmospheric pressure, p_{atm}, acting as a stress normal to the ice surface, $\boldsymbol{\sigma n_s}$, is negligible with regards to its effect on ice flow. We also allow our glacier surface to freely evolve in order to investigate elevation change. The height of the upper free surface of the glacier, z_s, is governed by an advection equation

$$\frac{\partial z_s}{\partial t} + u_s\frac{\partial z_s}{\partial x} + v_s\frac{\partial z_s}{\partial y} - w_s = a_s, \tag{8}$$

where $\boldsymbol{u_s} = (u_s, v_s, w_s)$ is the surface velocity vector given by the Stokes equation (Equation 3) and a_s is the accumulation or ablation component prescribed in the direction normal to the surface (Gagliardini et al., 2013). The accumulation and ablation term we apply in our BBGS simulations is given by Equation 2.4 and is applied temporally uniform throughout the quiescent experiments. The input surface height, z_s, to the quiescent simulations is given by the CryoSat-2 TFMRA Summer 2016 DEM (see Section 2), while the input surface height for the surge phase is given by the end-of-quiescence surface elevation result from the quiescent phase modeling experiment.

3.3.2 Ice-Bed Boundary and Friction Representation

The ice-bed boundary condition specifies a friction, or sliding, representation that specifies the relationship between basal shear stress and basal velocities and is an important aspect of modeling surge behavior (B. Kamb, 1970; Clarke et al., 1984; W. B. Kamb, 1987). In this section, we cover both the linear friction law used in modeling the quiescent phase and spatiotemporally evolving representation for the surge phase. The surge phase friction representation is an extension of the linear friction law and is designed to represent the evolution of a surge wave, or "surge front", that propagates down-glacier during the surge along the central flowline of the glacier.

We estimate the unknown basal friction law parameters through model-data comparisons of crevasses and surface velocities as described for the early-2011 portion of the latest surge in Trantow and Herzfeld (2018) and for the early quiescent phase (2014-2016) in Trantow (2020). By estimating these parameters using observations, we essentially bypass the need to explicitly model the basal water pressure responsible for the changing basal motion. Some friction laws allow one to infer the basal water pressure after estimating the unknown parameters (e.g. Jay-Allemand et al. (2011b)). A lack of hydrological observations for the BBGS makes these inferences difficult, however we attempt to describe basal conditions in relation to water storage and drainage efficiency based on the modeled mass redistribution and inferred hydropotential (see Section 3.4).

We begin by introducing aspects common to both the quiescent and surge basal friction representations. For each, we assume ice flow does not penetrate the basal boundary, that is, there is no normal component to ice velocity at the base

$$\boldsymbol{u} \cdot \boldsymbol{n_b} = 0 \tag{9}$$

where $\boldsymbol{n_b}$ is the unit surface normal vector pointing outward to the bedrock surface (Gagliardini et al., 2013).

3.3.2.1 Linear Friction Law for the Quiescent Phase

Basal motion in the direction tangent to the basal surface normal takes place throughout the entire BBGS system during most of the surge cycle, aside from a short (~1 year) time period immediately after the surge ceases and basal water pressures are fully relieved. The dynamics during this short time period can fully capture observed ice velocities in Lower and Central Bering Glacier by using a no-slip boundary condition (Trantow, 2020), however, in our 20 year quiescent simulation for this paper assume basal sliding is occurring always and everywhere. Experimentation in Trantow (2020) and Trantow (2014) show mean basal motion during quiescent flow, throughout the entire glacier system, is approximated using a linear sliding law

$$\sigma_{nt_i} = \beta u_{t_i}, \quad for\ i = 1, 2, \tag{10}$$

which relates the basal shear stresses, σ_{nt_i}, to the basal velocities, u_{t_i}, through the linear friction coefficient β. A constant and uniform value of $\beta = 10^{-4}\ \frac{MPa \cdot a}{m}$ is used for quiescent flow as informed by velocity observations during quiescence (Trantow, 2014, 2020). The uniform prescription of β across the entire glacier system serves as a first-order approximation of the basal conditions during quiescence. It attempts to capture many of the physical effects on basal velocity in a single parameter, such as the inverse relationship with effective pressure (N) (Bindschadler, 1983), the effect of irregular beds and cavitation (Schoof, 2005), and any additional frictional forces (Hallet, 1981; Iverson et al., 2003).

Obviously, this representation is limited and we would not expect β to be uniform throughout the glacier. We show however, that this representation applied to quiescent flow matches observations quite well, and we suggest ways to improve the spatiotemporal distribution of β based on model results and observed quiescent velocities in Section 4.4.

3.3.2.2 Spatiotemporal Friction Representation for the Surge Phase

In this section, we derive an equation for basal friction during a surge that utilizes a representation of the kinematics of the surge wave. During a surge, the linear friction representation adequately captures the spatiotemporally-local behaviors of ice flow as shown in Trantow and Herzfeld (2018). That is, the linear sliding law accurately captures observed ice dynamics for an ∼20 km longitudinal segment of the glacier for ∼3 months. This spatiotemporal-segment of dynamics corresponds to the ice that is actively surging during the surge-phase evolution. We use this information, along with additional velocity observations, to derive a spatiotemporally evolving basal friction function for the surge phase that utilizes the linear relationship between basal shear stress and basal velocities. This amounts to finding a distribution for the linear friction coefficient that evolves in space and time, $\beta = \beta(x,t)$. Physically, this representation models the propagation of a surge front, which acts as an activation-wave that changes basal conditions, a la Fowler (1987). A lower value of $\beta(x,t)$ reflects reduced basal friction, simulating lower effective pressure and faster basal motion. We use observations of a propagating front prior to and during the latest BBGS surge in 2008-2013 to estimate parameters in the new spatiotemporally-varying friction representation that follows (Turrin et al., 2013; Trantow, 2020).

A schematic of the surge phase friction representation is given in Figure 6(a). The surge-phase friction representation is specified along a 1D central flowline, whose distance from the upper glacier boundary is given by x (see Figure 6(b)). Values for β throughout the 2D ice-bed interface in the model are given by the closest along-flowline point. For example, the associated β value in the model for point A in 6(b) would be given by its closest value along the flowline at $x = 120$, that is, $\beta_A \equiv \beta(x = 120)$ at all times t. Similarly, point B would take on the value of β equivalent to that at $x = 145$. A more complex representation of basal friction that includes variations in the transverse direction (perpendicular to x) may be needed to capture the peculiar glacier flow observed in Central Bering Glacier during a surge, which manifest as branches in the flow regime divided by the deep central glacier trough (Herzfeld, McDonald, Stachura, et al., 2013; Trantow, 2020).

Mathematically, surge-phase basal friction is represented by a spatiotemporally evolving linear friction coefficient, $\beta(x,t)$, along the entire flowline axis (x):

$$\beta(x,t) = \begin{cases} \beta_{min} + (\beta_q - \beta_{min})\frac{x_{lead}(t)-x}{x_{lead}(t)-x_{trail}}, & if \quad x_{trail} \leq x \leq x_{lead} \\ \beta_q, & otherwise \end{cases} \tag{11}$$

for $t > 0$, with $t = 0$ corresponding to the time of surge initiation where basal conditions are given by the end-of-quiescence state. Parameters include a minimum linear friction coefficient, β_{min}, corresponding to the peak surge velocity, a linear friction coefficient corresponding to unactivated ice, β_q, equivalent to the associated quiescent phase value, and the leading edge, $x_{lead}(t)$, and trailing edge, $x_{trail}(t)$, of the actively surging region at some time t, which are governed by the surge front propagation speed, u_{front} and the surge wave initiation location x_{init}.

A formula for u_{front} is given by Fowler (1987) in terms of heights and velocities for each edge of the surge front. In our implementation of the surge wave here however, we assign a fixed propagation speed of 40 m/day which is on par with the observed propagation speed of the kinematic wave of 38.1 ± 5.5 m/day from 2008-2010 through Bering's trunk and into the lobe area (Turrin et al., 2013). Characteristics of the glacier at the

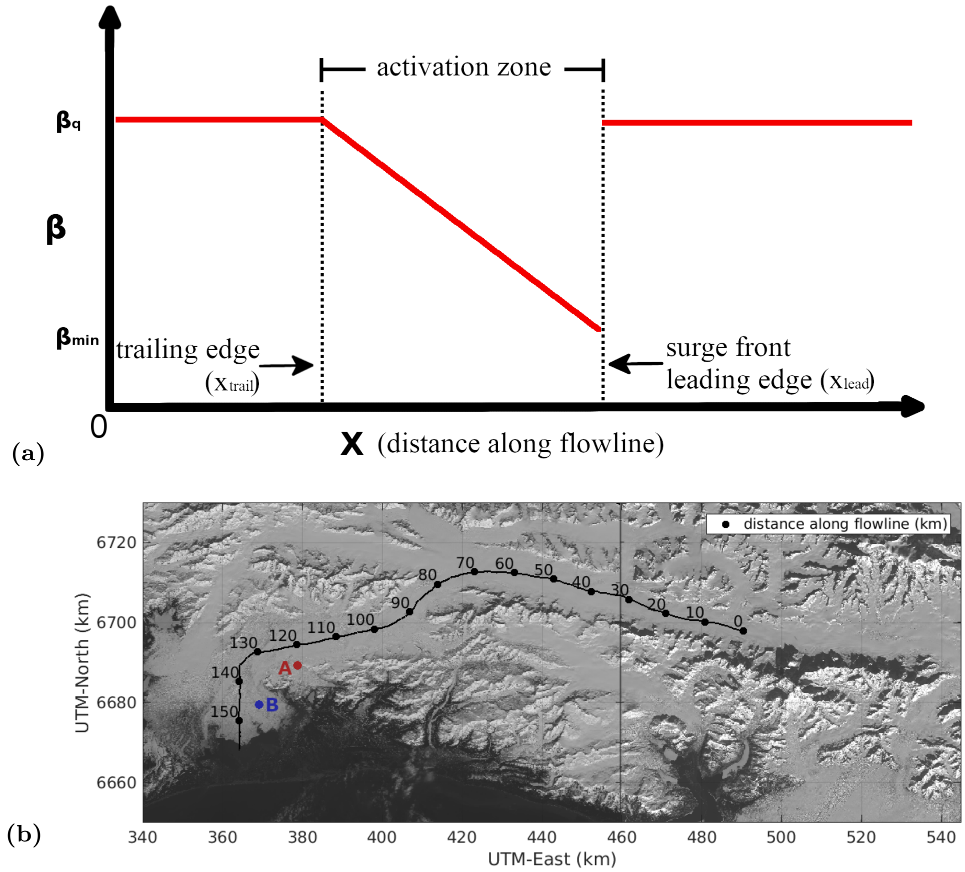

Figure 6. Linear basal friction coefficient distribution during the surge phase along the central flowline of the BBGS. (a) A schematic of the surge-phase friction representation at some time, t. The basal friction coefficient, β, is plotted versus along-flowline distance, x, where $x = 0$ is the uppermost location in the Bagley Ice Field. The actively surging ice within the activation zone is bounded by a leading edge, x_{lead}, and a trailing edge, x_{trail}, which evolve in time as governed by properties of a simulated surge wave. (b) The central flowline of the BBGS measured in km from the uppermost boundary in the BIF. β values at points away from the center flowline are given by its associated value at the closest point on the center flowline, e.g., $\beta_A \equiv \beta(x = 120)$ and $\beta_B \equiv \beta(x = 145)$ at any time t. For reference, the Bagley Ice Field stretches from km-0 to the Bering-Bagley Junction (BBJ) at km-80. Upper Bering roughly corresponds to segment of Bering Glacier from km-80 to km-100, Central Bering from km-100 to km-130 and Lower Bering (or the Bering Lobe) from km-130 to km-156 at the terminus. Most of the interesting surge dynamics occur in Bering's main "trunk" which stretches from km-80 to km-135.

end of quiescence will inform a choice of a surge initiation location along-flowline x_{init} (see Section 5.1).

With the surge wave propagation speed and the initiation location we can define the bounds of an activation zone of actively surging ice, given by the leading and trailing edge locations, at any time during the surge phase: $x_{active}(t) = x \in [x_{trail}(t), x_{lead}(t)]$. The location of the leading edge of the surge front is given by:

$$x_{lead}(t) = x_{init} + u_{front} \cdot t \quad (12)$$

where t is simulation time in years. Based on velocity observations of the surge front propagation in Turrin et al. (2013), we set $x_{trail}(t) = x_{init}$ for all times t since velocities appear to be elevated in Upper Bering Glacier throughout the initial surge phase from 2008 through 2010. Therefore,

$$x_{trail} = x_{init} \quad (13)$$

Ice up-glacier and down-glacier of the activation zone is considered "unactivated ice" and is assigned the quiescent phase value for the linear friction coefficient, β_q.

The final part of defining of basal friction coefficient during the surge-phase is given by the distribution of the β values within the activation zone. Observed surface speeds are largest near the leading edge, being significantly higher than the unactivated ice immediately down-glacier of the edge, and generally decrease as you move up-glacier (W. Kamb et al., 1985; Fowler, 1987; Raymond et al., 1987). By estimating linear friction values from observed surface velocity data from the 1982-1983 surge of Variegated Glacier, Jay-Allemand et al. (2011b) found the β distribution within the activation zone resembled a normal curve whose peak was near the leading edge. At some times during the surge, the estimated β distribution contained an additional peak up-glacier of the leading edge, which Raymond et al. (1987) suggest is due to irregularities in the bedrock topography. Based on the longitudinally-linear discrepancies in surge velocities between model and observations in Lower Bering in Trantow and Herzfeld (2018), we decide to use a simple linear distribution of β within the activation zone. We assign the minimum friction coefficient at the leading edge of the surge front, β_{min}, and have β linearly increase throughout the activation zone until its end at the trailing edge where the friction coefficient is set to its quiescent value, β_q.

The friction law applies to the entire surge phase but will only be tested for the initial surge phase in this paper due to computational limitations mentioned above (Section 3.1). Our simulations use a quiescent friction coefficient of $\beta_q = 10^{-4}\ \frac{MPa \cdot a}{m}$ based on results from Trantow (2014). The surge front basal friction coefficient value, β_{min}, is set to $\beta_{min} = 10^{-5}\ \frac{MPa \cdot a}{m}$, which comes from a result of optimizing the linear basal friction coefficient for the surge front in early-2011 (Trantow & Herzfeld, 2018). The linear transition between the two values within the activation zone describes an approximation of the observed surge progression during the latest surge, as mentioned previously. A diagram of the basal friction coefficient distribution within the activation zone is given in Figure 6(a).

3.3.3 Lateral Boundary

The material similarity of the glacier's base and margins (Koehler & Carver, 2018) leads to a prescription of the linear friction law at the lateral boundary as well. Experimentation in Trantow (2014) suggests the lateral friction coefficient, $\beta = \beta_{lat}$, is 5 times larger than the nearest basal sliding coefficient based on observed velocities and shear behavior near the margins.

We treat the lateral margins uniformly throughout the entire glacier perimeter by assuming a rigid, mountainous boundary (with or without till). This representation, however, does not hold for behavior at the glacier terminus. Calving at Bering Glacier's terminus is a complicated process somewhat unique among surge-type glaciers in that it calves into a series of proglacial lakes, the largest of which is Vitus Lake, rather than the ocean. Throughout most of the surge cycle, the terminus is grounded at the lake bed being prevented from floating like an ice-shelf by the tensile strength of the ice (Lingle et al., 1993). Unbalanced hydrostatic pressure acting on the glacier bottom pushes upwards at the glacier front resulting in a bending moment. The bending moment causes a fracture, likely at the point of maximum moment occurring at the glacier base, eventually leading to calving events. Since Bering Glacier is grounded below hydrostatic equilibrium, the icebergs pop up once calved, and float at a higher elevation than the grounded ice at the terminus. The calving mechanism occurring during the surge phase is unknown but likely takes the form of an active calving cliff (Lingle et al., 1993).

We do not model Bering's complicated and changing calving process in this paper and instead treat mass loss from the system due to calving in the following manner. First, we extend the glacier model domain by several kilometers (2-5 km) at the glacier terminus assigning it the minimum ice thickness of 1 meter as required by the model. The assumed true glacier terminus is derived from satellite imagery in 2016, marked by a solid black line in Figure 7, while the extended model boundary is given by observations of the terminus at its maximal extent after the most recent surge (Trantow, 2020). We treat all ice-mass that crosses into this extended region as ice lost to the system via calving. During the surge, the ice movement into this region may be seen as an approximate representation of terminus extension, but without a retarding force due to lake water. The latest surge extended Bering's terminus 2-4 km (Turrin et al., 2013), therefore our region of minimum ice thickness is large enough to account for this phenomenon.

3.4 Hydropotential as a Proxy for Subglacial Drainage Paths

Observations of subglacial hydrological systems are sparse, difficult to interpret and often do not provide the necessary information required to constrain parameters in a subglacial drainage model (Andrews et al., 2014; Brinkerhoff et al., 2016; B. de Fleurian et al., 2018). Moreover, there are very few applications of subglacial hydrological models to real topographies and forcings due to the modeling difficulties (B. de Fleurian et al., 2018). The absence of any comprehensive hydrological measurements for the BBGS, combined with the difficulty of applying a sophisticated subglacial hydrological model to a large and complex glacier system, led us to use a calculation of hydraulic potential (henceforth referred to as hydropotential) and its gradient to infer characteristics of the subglacial hydrological system throughout the surge cycle. The hydropotential does not have to be explicitly modeled as its calculation comes directly from glacier geometry after a few assumptions are made.

In this study we use the Shreve Potential (Equation 15) (Shreve, 1972) to estimate hydropotential and investigate evolution of glacial hydrologic characteristics throughout the surge cycle. More specifically, the gradient of hydropotential (hydraulic gradient) is used as a steady-state proxy for water flow. Water is estimated to flow from areas of high to low hydropotential in the direction of the (negative) hydraulic gradient. This approach has had success in predicting actual subglacial hydrologic characteristics (e.g., M. Sharp et al. (1993); Chu et al. (2016)). However, the calculation and subsequent analysis of the Shreve Potential requires several assumptions that are perhaps unrealistic for actual glaciers, which we discuss here as we introduce the mathematics.

Given a certain glacier geometry, the hydropotential is calculated by knowing the ice thickness and water pressure at some point within the glacier. The expression for hydropotential Φ at the bed is given by,

$$\Phi = \rho_w g z_b + p_w \tag{14}$$

where ρ_w is the density of water, z_b the elevation of the bedrock and $p_w = \rho_i g h - N$ the water pressure with ρ_i representing ice density and N effective pressure. N takes positive values during quiescent flow, with smaller values corresponding faster flow, and approaches zero during a surge (Fowler, 1987; Benn et al., 2019). If we assume p_w to be some fraction $0 \leq \chi \leq 1$ of the ice overburden pressure, $p_i = \rho_i g h$, then hydropotential can be calculated by,

$$\Phi = \rho_w g z_b + \chi \rho_i g h \tag{15}$$

Using this representation for hydropotential, we see that the higher the water pressure, the more glacier thickness h effects the water drainage path relative to the topography of the bedrock, given by z_b, which governs how water drains in the absence of overburden ice. Similarly, if χ is held constant, Equation 15 implies that a local increase in h leads to a χh increase in local water pressure and therefore a $(1-\chi)h$ increase in local effective pressure.

Observations from nearby Columbia Glacier, a fast-moving temperate glacier ∼220 km northwest of the BBGS, estimate water pressure ranging from ≈93% of the ice pressure near the terminus during its fastest observed velocity in 1984, down to ≈40% of the ice pressure up-glacier from the terminus during its slower movement in 1977 (Meier & Post, 1987). Observed velocities in 1977 were around 0.4 m/day in 1977, and increased to almost 2 m/day by 1984 (Meier & Post, 1987). This range is similar to the range of mean surface velocities observed across the BBGS during quiescence (see Section 4.4), and it is thereby reasonable to assume similar effective pressures for the BBGS.

Therefore, for calculations in the following sections, we calculate hydropotential using a spatially uniform χ with bounds of 0.4 to 0.93 for the majority of the quiescent phase, and $\chi = 1$ ($N = 0$) for surge initiation at the end of quiescence and during the surge phase itself. With $N = 0$, it is assumed that water completely fills the subglacial (or englacial) drainage conduit, while the uniformity assumption implies that the enlargement rate of the conduit is the same at every location.

In addition, the uniformity assumption implies: (1) the glacier ice and subglacial till have an intrinsic permeability that is homogenous and isotropic, and (2) the recharge of water to the glacier bed is spatiotemporally uniform (Gulley et al., 2009, 2012). The spatiotemporal heterogeneity of both subglacial water recharge, i.e., water entering the subglacial drainage system, and hydraulic conductivity at the glacier bed have both been identified by Gulley et al. (2012) to be important components of estimating hydropotential, and they are not accounted for in the formulation of Equation 15. However, given our available data sets and the usefulness the Shreve potential approach to estimate subglacial drainage characteristics in some previous studies (M. Sharp et al., 1993; Chu et al., 2016), we proceed to estimate hydropotential using Equation 15 keeping in mind its assumptions and limitations.

4 The Quiescent Phase

Prognostic simulations of the entire quiescent phase help identify how mass is redistributed in the BBGS over the course of normal flow, which leads to conditions favorable for surging. After providing some model specifics for the quiescent simulation, we analyze the mass redistribution results and estimate mass loss over 20-years of quiescent flow (Section 4.1). Next we infer changes in the basal hydrological system caused by the mass redistribution through calculation of the subglacial hydraulic gradient (Section 4.2). We then identify reservoir areas and associated subglacial topography characteristics that are responsible for the observed changes in Section 4.3. Finally, we compare simulated and observed velocity during quiescence and propose a way to increase complexity of the quiescent phase friction law to better match observations in Section 4.4.

We simulate quiescent flow for 20 years using 10-day time increments (730 total time steps), which corresponds to the approximate length of the observed BBGS quiescent phases since 1900 (B. F. Molnia & Post, 2010a). While the most recent quiescent phase, beginning in 1996, lasted only 12-15 years, the results in this section remain applicable as changes during quiescent flow are gradual and evolve monotonically. The magnitude of changes expected during the last full quiescent phase however, might not be as dramatic as the 20-year results given in this section.

4.1 Elevation Change and Mass Loss

Figure 7(a) shows modeled quiescent elevation change by differencing the initial surface elevation with the surface elevation after 20 years of evolution. The initial ice surface is taken as the glacier surface after 50 time steps of free evolution in order to reduce any elevation-change signals arising from errors in the input surface DEM (Trantow et al., 2020).

Figure 7(b) shows the approximate contribution of SMB forcing on the overall quiescent elevation-change signal. The approximation is calculated by applying the SMB rate to the initial topography aggregated for 20 years. The true SMB signal changes at each time step due to a redistribution of ice-surface elevation with the gravity-forced dynamics tending to move ice to lower elevation, and therefore this approximate SMB elevation-change signal has a slight positive bias. With total mean elevation changes of -16.77 $\pm$ 72.25 m in Figure 7(a), the estimated SMB signal would have an approximate error of -0.027 $\pm$ 0.12 m compared to the true SMB signal that changes at each time step (see Equation 2.4).

With our enforced accumulation/ablation pattern based on observations in the current realm of climatic warming, it is not surprising that the overall glacier system loses mass. We see accumulation up to 20 m throughout most of the Bagley Ice Field with significant melt rates throughout Bering Glacier and the lower Bagley exceeding 30 meters near Bering's terminus. These rates lead to a total estimated volume loss signal of 25.21 km^3 from SMB over the 20-year simulation (1.363 km^3 per year).

Subtracting the SMB signal from the total simulated elevation-change we receive the dynamic-residual, i.e., the elevation change signal from the dynamics of the glacier (Figure 7(c)). Clearly, the pattern of elevation-change is dominated by the dynamics of the glacier which is expected for the relatively fast-moving temperate glaciers of southeast Alaska. Ice loss due to dynamics comes in the form of calving which we estimate as mass passing past the flux-gate marking the initial terminus (black line in Figure 7(c)) and into the extended region at the front of the glacier (see Section 3.3.3). Over the course of the 20 year quiescent phase, we estimate 12.88 km^3 of volume loss due to calving in the BBGS (0.644 km^3 per year). Thus, the combined volume loss is approximately 38.09 km^3 for 20 years (1.90 km^3 per year) with SMB contributing to 2/3 of the signal and volume loss due to dynamics (calving) contributing to 1/3.

The SMB estimate on Bering Glacier alone is -28.12 km^3 (-1.41 km^3 per year), which is larger than the net SMB for all of the BBGS due to the primary accumulation zone being above Bering Glacier in the Bagley Ice Field. In addition, all of the BBGS ice loss associated with the dynamics (calving) can be prescribed to ice-loss from Bering Glacier since ice exists the system at its terminus in Vitus Lake. This gives a combined volume loss estimate of -41.00 km^3 (2.05 km^3 per year).

Converting these volume estimates to mass loss estimates is not straight forward due the presence of crevasses (volume-voids in the ice mass) and density variation in the firn (R. P. Sharp, 1951; Huss, 2013), which would significantly effect mass loss estimates from SMB. Temperate firn has a depth that usually depends on elevation and can exceed 10 m on glaciers similar to the BBGS (R. P. Sharp, 1951; Arcone, 2002). The av-

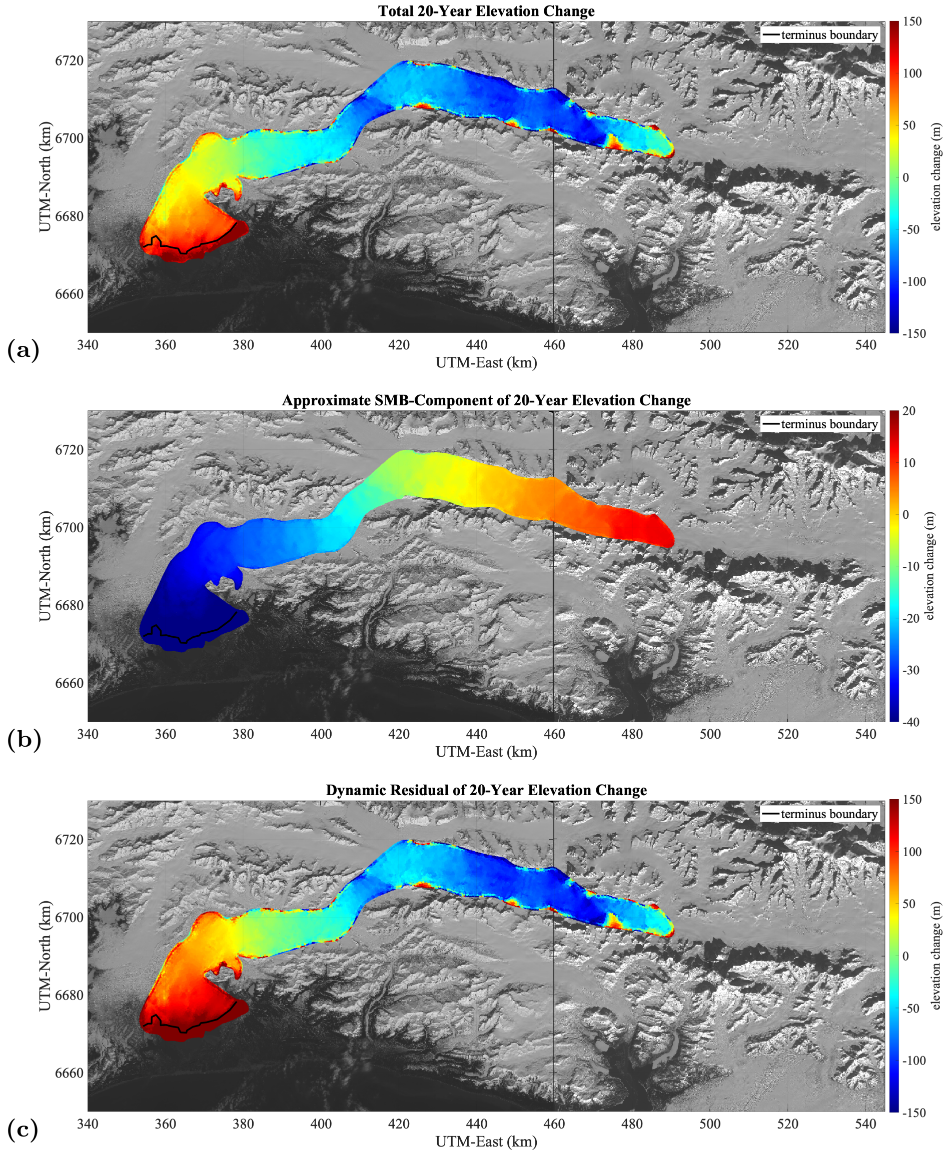

Figure 7. Elevation change results from 20-year quiescent simulation of the BBGS. (a) Total elevation change in meters. (b) Approximate SMB component of elevation change. (c) Approximate dynamic component of elevation change. The black line marks the assumed glacier terminus, derived from the observed 2016 boundary, and is treated as a flux gate to estimate calving.

erage firn density, found at a few meters depth, is approximately 700 kg/m^3 for temperate glacier ice near the St. Elias Mountains like the BBGS (R. P. Sharp, 1951). Adopting this average value to convert the Bering Glacier volume loss estimate to mass loss for the SMB component gives 19.68 Gt over 20 years (0.98 Gt per year). Mass loss from dynamics (calving) assumes a full glacier ice density of 917 kg/m^3, as the firn component is negligible due to its limited depth compared to the overall glacier thickness at the terminus (upwards of 400 m, Figure 4(c)). Thus, the ice mass loss due to calving is estimated at 11.81 Gt (0.590 Gt per yr). Together, our model's estimate of mass loss from Bering Glacier is -31.50 Gt over 20 years of quiescent flow (-1.57 Gt per year).

Mass balance numbers given by Larsen et al. (2015) estimate that Bering Glacier mass loss is 2.73 Gt per year based on lidar observations from 2000-2013. While our estimate is significantly lower, the time range in Larsen et al. (2015) covers the majority of the latest surge where signifiant mass loss would be experienced through dynamic components (e.g., calving). While we do not provide mass loss estimates during the surge phase, assuming that our estimates are correct for the 8 years of quiescent flow from 2000-2008, mass loss may reach 4.59 Gt per year during the surging years between 2008 and 2013.

4.2 Hydropotential Analysis

We use hydropotential to infer characteristics of the subglacial drainage system that result from changing geometries, as described in Section 3.4. Maps of hydropotential provide estimates for the path that water takes through the ice-bed interface as it drains to the glacier terminus, flowing down the hydraulic gradient from high to low (hydro)potential.

The basal hydropotential depends on local ice thickness and can therefore deviate from the topographic gradient of the bedrock, that is, the accumulation of ice in reservoir areas during quiescence changes the drainage paths of subglacial water. In general, the steeper the surface slope, the less the glacial drainage flows along the local bed topography (Shreve, 1972). Therefore, we expect the glacier steepening near the reservoir areas to divert the flow of water at the base from its early-quiescent path.

While hydropotential maps are derived from modeling results in this section, they can also be derived simply from observations using a surface and bedrock DEM. We perform this observation-based analysis for the BBGS during (Summer 2011) and near the end (Summer 2013) of the surge in Section 5.3, owing to the availability of reliable CryoSat-2 data in the area beginning in 2011 (Trantow & Herzfeld, 2016). Hydropotential maps derived from a model are as accurate as those from observations in so long as they are able to accurately represent the surface elevation, or more importantly elevation-change since our model is initialized with observed topography. Trantow (2020) (Section 7.3) demonstrates the model's ability to accurately model elevation change in the BBGS, and therefore we expect the model-derived hydropotential maps to be as reliable as observationally-derived maps.

Figure 8 gives a full spatial map of the basal hydropotential of the BBGS in year-1 and year-20 of the quiescent simulation. Colored contours are given at 0.2 MPa intervals while black labeled contours are given at 1.6 MPa intervals. The general direction in which water flows will be perpendicular to the equipotentials of the hydropotential. Subglacial water storage occurs in closed areas of lower hydropotential (hydropotential wells), similar to ordinary lakes forming in closed areas of lower elevation (Shreve, 1972).

These maps indicate that the efficiency of the hydrologic drainage throughout Bering Glacier's trunk, given by the amount of contours per distance along the flowline, is much lower in year-20. The 1.6 MPa black reference lines are given in the figure to help highlight this change. Moreover, we see the development of potential wells throughout Bering Glacier as indicated by the arrows in Figure 8(b). The formation and expansion of hydropotential wells indicates increased water storage capacity as the quiescent phase matures. The development of hydropotential wells is most clear in the 2D contour maps of Figure 8 when assuming larger values for χ, and we therefore set $\chi = 1$ for these maps.

To better visualize and quantify these subglacial drainage changes in Bering Glacier's trunk, we created along-flowline plots of the hydropotential and hydraulic gradient by averaging the values across the glacier width. Figure 6(b) gives a reference to the along-flowline distance starting at the uppermost accumulation zone near the Eastern Bagley Ice Field's confluence with Columbus Glacier, and ending ∼157 km down glacier at Bering's

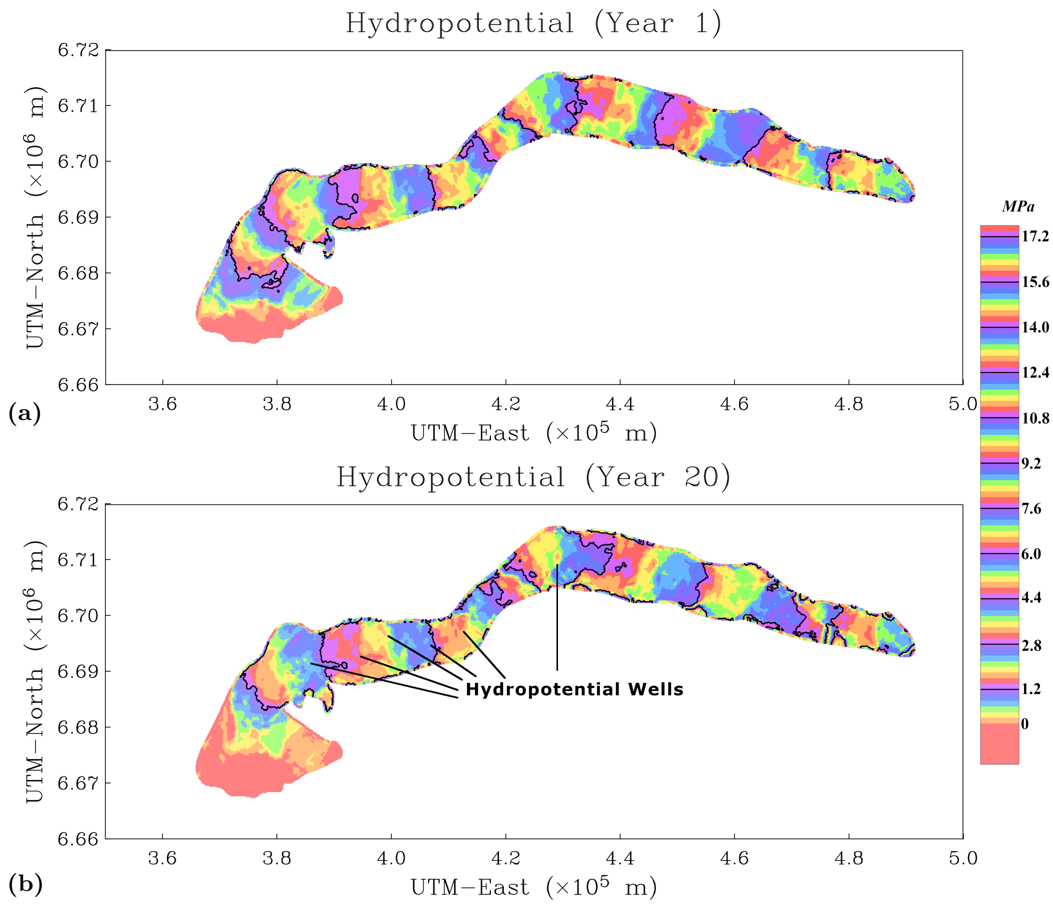

Figure 8. Modeled basal hydropotential for at the beginning and end of the 20-year quiescent phase simulation of the BBGS. Colored contours are given at 0.2 MPa intervals while black-lined contours are given at 1.6 MPa intervals. (a) Basal hydropotential for at the beginning of the quiescent phase in year 1. (b) Basal hydropotential at the end of a 20-year quiescent phase. The black lines indicate notable hydropotential-wells that have grown or developed over the course of 20-years of quiescent flow. Both maps assume zero effective pressure ($\chi = 1$).

terminus. Note however, that labeling this the flowline is somewhat misleading as several flow regimes exist and multiple subglacial troughs divide the flow across the glacier width, especially near the lobe area past the 125 km mark (B. F. Molnia & Post, 2010a; Trantow, 2020).

These plots assume that water drains across an entire given transect, however, the water flux across the transect will likely vary. For example, most water would likely drain through a narrow trough near the glacier center, with less water crossing the transect near the glacier margins. Our hydropotential analysis assumes that water input to the glacier system is in a steady state (Section 3.4), and therefore this type of width-averaged analysis compares the flow across a given transect relative to the same transect at a different time. These plots do not quantify the magnitude of the water flux across a transect, but instead provide insight into the changing tendency of efficient down-glacier flow compared to less-efficient transverse, or even up-glacier, drainage.

We investigate several cases based on possible water pressures given as a fraction of the overburden pressure, χ, which ranges from 0.4 to 0.93 based on observations from the nearby Columbia Glacier (see Section 3.4). We also look at the case when effective pressure is zero, $\chi = 1$, which is expected at the end of quiescence and at surge initiation.

Figure 9(a) shows the mean along-flowline elevation (dashed line) and hydropotential with high representative water pressure ($\chi = 0.93$, dotted line) and a low representative water pressure ($\chi = 0.4$, dashed-dotted line) at both the beginning (red) and end (blue) of the quiescent experiment over the trunk of Bering Glacier (km-80 to km-135). Hydropotential tends to vary more at lower water pressure, whereas at higher water pressures, the hydropotential profile begins to more closely resemble the glacier surface profile as expected from Equation 15 when the glacier surface height (or glacier thickness in general) begins to influence the drainage path more significantly.

It is the *difference* in hydropotential, across some fixed distance, that is the salient measure of hydraulic flow efficiency rather than the magnitude of hydropotential at some location. We therefore analyze the difference in hydropotential across Bering Glacier's trunk which decreases over the course of quiescence for each water pressure case. In the high water pressure case, $\chi = 0.93$, the difference in hydropotential across the trunk decreased by 16.0% while for low water pressure case, $\chi = 0.4$, the decrease was smaller at 10.4%. There is less of a decrease in the low pressure case since the hydropotential is less influenced by the changing glacier thickness and is more influenced by the fixed bedrock topography (Equation 15). Even without considering the existence of hydropotential wells, this result suggests that over the course of quiescence Bering Glacier's trunk evolves to drain basal water less efficiently down-glacier, with more transverse drainage paths, assuming a fixed water inflow rate and pressure.

In Figure 9(b) we provide a range for the basal hydraulic gradient profile during quiescence. We see that the hydraulic gradient takes on more extreme values, particularly in Upper Bering above km-105, when the water pressure is lower ($\chi = 0.4$) and the drainage paths are more closely aligned with the bed topographic gradient (Equation 15). A positive hydraulic gradient implies water flowing up-glacier (averaged across the glacier width), indicating a local storage in basal water.

With the accumulation of water, we would expect basal water pressures to rise (increasing χ values) resulting in drainage paths that give more weight to the local ice overburden pressure. As seen in Figure 9(b), a larger χ value results in a more uniform down-glacier flow, given by less variable hydraulic gradient values. Thus, the glacier can accommodate an increasing basal water pressure with more efficient down-glacier drainage. However, several locations remain where water tends to accumulate throughout quiescence no matter the basal water pressure, namely around km-97, km-102 and km-124 which we discuss further in the next section regarding reservoir areas. The locations of the reservoir areas remain the same independent of the value of χ.

Figure 9(c) shows the mean along-flowline hydraulic gradient of Bering Glacier's trunk over the course of quiescence (solid lines) with shaded areas reflecting locations where Bering Glacier is storing basal water, given by positive hydraulic gradients. Here we assume $\chi = 1$, as expected by the end of quiescence, to demonstrate the evolving hydraulic gradient independently of water pressure. We attain similar results for any fixed χ value.

Clearly, the amount of water being stored at the end of quiescence (shaded blue area) has increased significantly from the beginning of quiescence (shaded red area). The amount of water stored in the hydropotential wells, as estimated by the area of each line

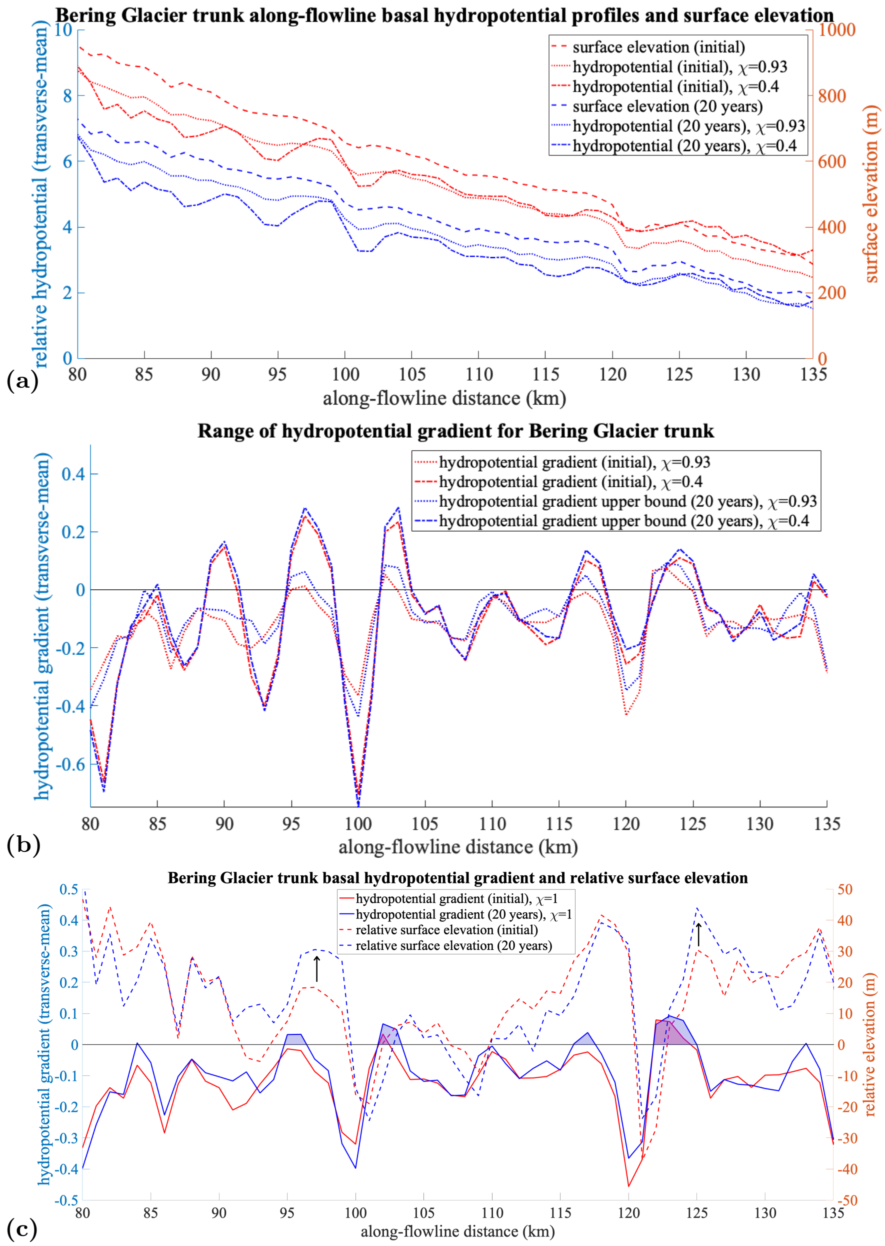

Figure 9. Change across the Bering Glacier trunk with regards to hydropotential and surface elevation over the course of the modeled quiescent phase. Red lines reflect the glacier state at the beginning of quiescence while blue lines reflect the end of quiescence state. (a) Hydropotential at high representative water pressure ($\chi = 0.93$, dotted lines and low representative pressures ($\chi = 0.4$, dashed-dotted line), together with the mean surface elevation profile (dashed lines). (b) A range of hydropotential gradients across Bering Glacier's trunk for the cases in (a). (c) Hydropotential gradient at zero effective pressure ($\chi = 1$, solid lines), representing the end-of-quiescence state, and relative surface elevation (dashed lines). Relative surface elevation is calculated by removing the mean slope of surface elevation. Shaded areas reflect locations where the hydropotential gradient is above zero implying water flowing up-glacier, i.e., subglacial water storage. Black arrows indicate growing surface bulges.

above zero, has increase by 246% over the course of quiescence. These well-areas, and other areas where the hydraulic gradient is less than zero along the flowline, correspond to the surge "trigger zones" identified in Robin and Weertman (1973) where basal water is "dammed" increasing stored water in the up-glacier zones where the hydraulic gradient is near-zero, which corresponds to the "collection areas".

The dashed lines in Figure 9(c) show the relative elevation initially (red) and after 20-years of quiescent flow (blue). Relative elevation is found by subtracting the mean slope from the elevation profiles in Figure 9(a) and indicates where reservoir areas, or surface bulges, are forming. The black arrows around km-97 and km-123 indicate building reservoir areas, while the high relative-elevation area around km-118 retains a fixed magnitude throughout the quiescent phase while steepening on it's up-glacier-side. The enlarging reservoir areas and steepening of local geometry lead to increased stored water in the areas 2-4 km up-glacier of these bulges. We also identify an area of stored water around km-102 without a large corresponding surface bulge, however, the relative surface slope in this area is steepening due to local bedrock characteristics as we shall see in the following section.

In summary, our hydropotential analysis for the quiescent phase shows that when basal water pressure is lower (smaller values of χ), (positive) hydropotential gradients are larger while the hydropotential difference across the glacier's trunk is smaller. Therefore when basal water pressure is lower during quiescence, there is slower, less efficient drainage and more basal water is present across the length of the Bering Glacier trunk where most of the surge activity occurs. Even when χ is at its maximum value of one, representing zero effective pressure, locations of positive hydropotential gradients remain present and are enlarged by the formation of reservoir areas during the course of quiescent flow (Figure 9(c)). Therefore, independent of the choice of χ, positive hydraulic gradients are always present during quiescence at several key locations, which, as we discuss in the next section, coincide with potential bedrock-controlled trigger areas for various stages of a BBGS surge.

4.3 Reservoir Areas and Bedrock Topography

The locations of the reservoir areas, along with the basal water storage areas, are attributed to the characteristics of Bering Glacier's bedrock topography, shown in Figure 10(a), whose shape is influenced by the local faults (Koehler & Carver, 2018; Trantow, 2020). In particular, it is the extension of the surrounding mountain ridges underneath the glacier, termed "subglacial ridges", that are responsible for damming ice at these locations. Black arrows in Figure 10 point out some of the significant subglacial ridges. Directly up-glacier of these ridges are local deepenings in the basal topography where water collects. Ice-mass build-up in front of these deepenings, caused by the subglacial ridges, slows the down-glacier drainage resulting in increased water retention in this area as shown in Figure 9(b).

The three reservoir areas we have identified through our quiescent phase simulation are circled in red in Figure 10(a) and the four areas of subglacial water storage are circled in dark purple. These areas are possible locations where surge initiation (or re-initiation) occurs, likely at the down-glacier edge of the reservoir areas where ice-surface geometry is steepest (Fig. 10(a)). The reservoir area centered at km-97 with a leading edge at km-100, termed RA-97, is identified by Burgess et al. (2013) to be the reservoir area for the initial surge phase in early-2008, which, after mass transfer to the receiving areas, likely caused the observed rift in the former receiving area (Herzfeld, 1998; Herzfeld, McDonald, Stachura, et al., 2013; Trantow, 2020). D. R. Fatland and Lingle (2002) hypothesize that RA-97 is the reservoir area for the 1993-1995 surge of Bering Glacier. RA-97 is formed by two transverse pairs of subglacial ridges just up-glacier of Ovtsyn Glacier on the north margin and just down-glacier of Kuleska Glacier on the south margin. Ice-mass accumulates behind the ridges, filling the deep bedrock depression, giving the thickest ice in all of Bering Glacier.

The reservoir area centered at km-124 with a leading edge at km-126, termed RA-124, is identified as the reservoir area in 2010/2011 by Herzfeld, McDonald, Stachura, et al. (2013) for the major surge phase occurring in early 2011, who measured a prominent surface lowering at this location of over 50 m in the summer of 2011 indicating a bulge collapse after the surge had been progressing for several months. Down-glacier of RA-124 in the Bering lobe is an area of complex topography where the deep trough running through Bering's trunk splits into two major branches, which we term the Tashalish Trough in the west and the Grindle Trough in the east, with even more subglacial troughs appearing further down-glacier in the lobe area. The Khitrov and Grindle Hills on the north and south side of the glacier respectively, produce large subglacial ridges that serve to accumulate ice before it crosses the Khitrov-Grindle line by flowing down a particularly steep section of bedrock into the lobe area. This steep slope, identified along the Grindle Corner in aerial imagery by a series of ice falls (Herzfeld, McDonald, Stachura, et al., 2013; Trantow & Herzfeld, 2018), explains why the surge wave, as measured by Turrin et al. (2013), speeds-up once it reaches this area.

Subglacial ridges that continue from nearby mountain ridges are also frequent in the Bagley Ice Field, as seen in Figure 10(b), causing ice-mass build-ups directly up-glacier (specifically near km-64, km-41, km-31, km-23, km-12 and km-3). Their existence in the BIF is evident from the topographically induced en-échelon crevasses (Figure 3(f)) (Herzfeld & Mayer, 1997; Herzfeld et al., 2004; Herzfeld, McDonald, Stachura, et al., 2013).

The Bagley Ice Field does not experience a full-scale surge of its own due in part to a lack of significant melt-water throughout all but the lowest parts of the ice field (Herzfeld, McDonald, Stachura, et al., 2013). As seen in our SMB prescription (Figures 5 and 7(b)), along with Larsen et al. (2015), most of the Bagley Ice Field lies in the accumulation zone of the glacier system and experiences minimal surface melt throughout the year. The lower part of the Bagley Ice Field does experience significant melt with a net-negative SMB balance down-glacier of km-60. The reservoir area at km-64 (RA-64) coincides in location with a small acceleration event (mini-surge) identified by Burgess et al. (2013) that occurred in the Bagley Ice Field during quiescence in 2003. Based on the local basal topography, the released basal water during the mini-surge event would divert northwest through Tana Glacier, quickly exiting the subglacial drainage system, and little basal water would be expected to flow across the BBJ into Bering Glacier. Tana Glacier is significantly shorter and thinner than Bering Glacier, with shorter water drainage passageways, and can evolve more readily to accommodate up-glacier changes in mass and water flux. Tana Glacier is not a surge-type glacier (Lingle & Fatland, 2003; Burgess et al., 2013), and thus mass imbalances and water retainment likely do not occur on the scale that they do in Bering Glacier.

Lingle and Fatland (2003) describe velocities in the BIF during the 1993-1995 BBGS surge using SAR interferometry and found a large "bullseye" at the location of RA-64. The bulls-eye corresponds to englacial water build-up that had caused vertical motion in the glacier during the 1993-1995 BBGS surge. Due to RA-64's location just above the BBJ, hydrologic changes experienced here may have some affect on Upper Bering Glacier where the surge is thought to initiate.

4.4 Velocity Comparisons and Relation to Hydraulic Gradient

We compare modeled velocity to observed velocity during the quiescent phase in order to (1) check that our modeled velocity is close to observations and (2) use the differences to suggest ways to improve the quiescent phase modeling. Figure 11(a) gives the observed mean annual velocity across the BBGS from 2020-03-08 to 2021-03-03 as

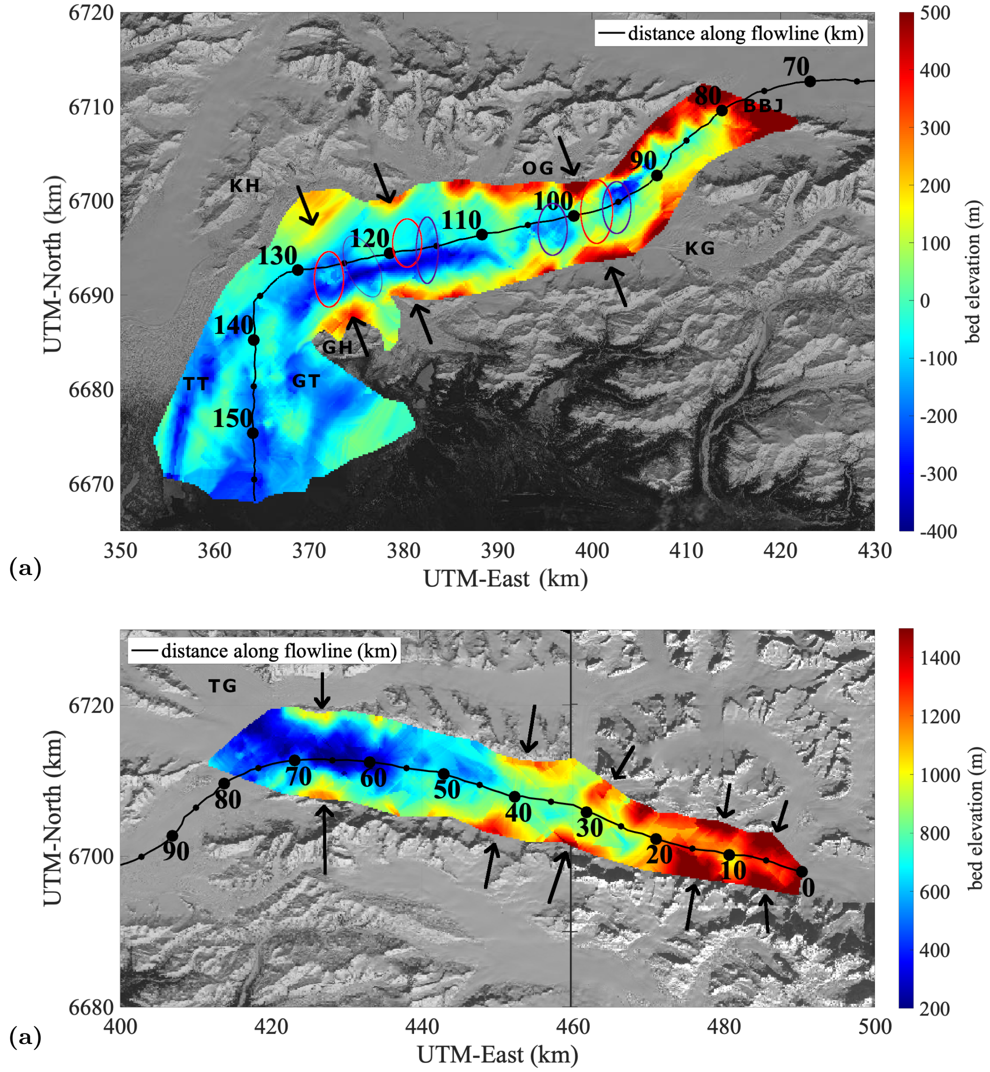

Figure 10. Locations of estimated reservoir areas and water storage over bedrock topography for Bering Glacier and the Bagley Ice Field. The along-flowline distance is given by the black line (km) while black arrows indicate subglacial features that contribute to the formation of the reservoir areas. a) Bering Glacier bedrock topography. Possible reservoir areas are circled in red and water storage areas are circled in dark purple. (b) Bagley Ice Field bedrock topography with notable subglacial ridges indicated by arrows. BBJ – Bering-Bagley junction, TG – Tana Glacier, KG – Kuleska Glacier, OG – Ovtsyn Glacier, TT – Tashalish Trough, GT – Grindle Trough, KH – Khitrov Hills, GH – Grindle Hills. The bedrock topography comes from JPL-WISE measurements (Rignot et al., 2013) that were interpolated to a DEM for the model (Trantow & Herzfeld, 2018).

derived from Sentinel 1A imagery using the SNAP toolbox (provided for analysis of SAR data by ESA,(Veci et al., 2014)). Around 90% of the glacier system moves at a rate less than 1 m/day, but there are pockets of accelerated flow throughout that exceed 2 m/day with max speeds reaching 5 m/day in Central Bering Glacier. These pockets coincide with the areas of water retainment identified in the previous section. This result suggests that the observed acceleration pockets are correlated with local hydrologic drainage inefficiencies leading to low effective pressures. Maps during other years of quiescence show similar patterns (Trantow (2020), Chapter 4.2).

Figure 11(b) gives the modeled velocity near the end of quiescence at the same scale as the observed velocity in (a), and Figure 11(c) shows the observed velocity minus the modeled velocity with a mean difference of -0.21 $\pm$ 0.63 m/day across the BBGS. Similar to observations, our model predicts that 93% of the glacier moves slower than 1 m/day, with areas of accelerated flow. The areas of accelerated flow however, do not directly coincide with observations, which is likely due to the use of a uniform friction law that doesn't account for spatial variability in effective pressure. One possible way to account for the variability in pressure within the quiescent phase friction formulation is to use the hydraulic gradient as a proxy for effective pressure.

Figure 11(d) plots the along-flowline velocity difference (blue) averaged across the glacier width versus the smoothed hydraulic gradient along-flowline (red) at the end of quiescence ($\chi = 1$). The hydraulic gradient is smoothed across a 5 km length to avoid high frequency signals that may result from errors in the basal topography. The 5 km length was chosen to match the approximate size of the dominant basal features, i.e., the troughs, throughout Bering's trunk. We see that the hydraulic gradient at locations in Bering Glacier and lower Bagley, i.e. the ablation zone down-glacier of km-65, are correlated with the difference between observed and modeled velocity, which suggests that a linear relationship exists.

Places along-flowline where our model over-estimates surface velocity have corresponding dip in the local hydraulic gradient and vice versa. This correlation suggests the possibility for hydraulic gradient estimates to inform the spatial variability of a non-uniform friction coefficient for the quiescent phase. A general formulation of a friction coefficient that reflects this is given by,

$$\beta = \beta(\nabla\Phi) \tag{16}$$

where β is the linear friction coefficient from Equation 10. Note that an effective pressure relationship is assumed through the choice of χ in the hydropotential calculation (Equation 15). This formulation can be extended to the surge-phase friction representation as well (Equation 11), based on similar model-data velocity differences found in Trantow and Herzfeld (2018) during the early-2011 period of the latest BBGS surge.

While there is a consistent correlation between model-data velocity difference and the hydraulic gradient in the ablation zone, there is larger variability in the hydraulic gradient relative to the mean velocity difference in the accumulation zone, likely due to less basal water and a smaller χ value, implying that χ likely depends on the along-flowline location, x. In summary, these findings constitute an advance in the physical process understanding of basal sliding during a glacier surge cycle.

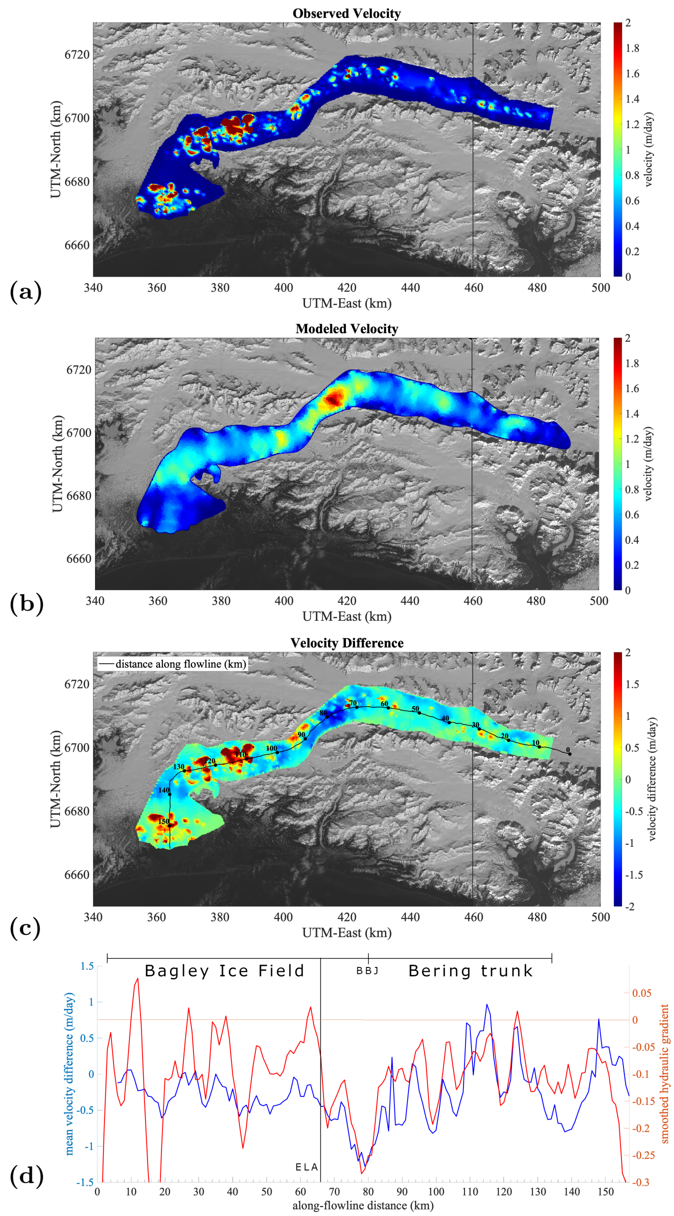

Figure 11. Observed and modeled ice-surface velocity during the BBGS quiescent phase. (a) Observed velocity derived from Sentinel-1 SAR imagery (S1A, 2020-03-08 and 2021-03-03). (b) Modeled velocity near the end of quiescence. (c) Observed-modeled velocity difference with along-flowline distance plotted in black (observed minus modeled). (d) Mean velocity difference (blue) and smoothed hydraulic gradient (red) along-flowline ($\chi = 1$). The black vertical line marks the equilibrium-line altitude (ELA) that divides the accumulation zone up-glacier and the ablation-zone down-glacier where significant amounts of melt-water exist during the melt season. The Bering Bagley Junction (BBJ) at km-80 marks the divide between Bagley Ice Field (km-0 to km-80) and Bering Glacier (km-80 to km-157) with Bering's trunk stretching from km-80 to km-135.

5 The Surge Phase

Here we model the ∼2-year initial surge phase as it progresses through the trunk of Bering Glacier (corresponding to the 2008-2010 phase of the most recent surge). A full-Stokes simulation of the full surge phase that includes the second surge phase, most recently occurring in 2011-2013, is calculated more feasibly using high-performance computing which is left for future work. In the mean time, we supplement interpretation of the second surge phase and the return to quiescence using observed CryoSat-2 Digital Elevation Models and Landsat-derived velocity maps from 2011 and 2013 (Trantow & Herzfeld, 2016).

In this surge phase section, we begin by postulating a surge initiation criterion in Section 5.1 based on the results of the quiescent phase experiments which may serve to link quiescent and surge simulations in future experiments. Next, we present the results of our two-year surge-simulation of the BBGS's initial surge phase given by a surge wave propagating trough Bering Glacier's trunk in Section 5.2. We present results of modeled velocity (Section 5.2.1), basal shear stress (Section 5.2.2), elevation change (Section 5.2.3) and hydropotential (Section 5.2.4) at various time stamps throughout the simulation. Finally, in order to complete our picture of the surge past the initial phase, we use CryoSat-2 observations in Section 5.3 to analyze mass redistribution and hydrologic drainage efficiency during the 2011-2013 phase of the most recent BBGS surge (second surge phase) ending with the transition back to a quiescent state (Section 5.4).

5.1 A Surge Initiation Criterion for the BBGS

Surge initiation, or the surge trigger, refers to a sudden dynamic change in the flow state of the glacier. It is poorly understood and is likely more complicated than a single event in time occurring at a particular location (Meier & Post, 1969; Raymond, 1987; Harrison & Post, 2003). Predicting surge initiation based on the state of the modeled glacier is an interesting topic that may require a dedicated study of its own. Here we investigate our end-of-quiescent results to identify likely surge initiation locations and important parameters that can be used in a surge initiation criterion to connect a quiescent phase simulation with a surge phase simulation.

The traditional surge hypothesis states that surges are triggered due to an internal change in the system such as the collapse of a generally efficient drainage system (EDS) (Meier & Post, 1969; Clarke et al., 1984; Raymond, 1987; Harrison & Post, 2003). Trantow (2020) showed that surge initiation of the last three BBGS surges showed no clear correlation with nearby monthly precipitation and temperature anomalies, with respect to their decades-long average, as measured by the nearby Cordova weather station. Furthermore, an annually-averaged modeling approach like the one used in this study would not be able to resolve the exact seasonal timing of the surge, yet it is able to identify the secular trends in glacier geometry and hydrology that leave the glacier primed for surging for a given year. We therefore investigate only parameters associated with the glacier geometry and the basal drainage system, via hydropotential analysis, to postulate a possible surge-initiation criterion.

First, we can use our current quiescent phase model results to estimate locations for where the surge may initiate. A sudden change in drainage efficiency is likely to occur at locations with steep hydraulic gradients where water is least likely to accumulate and maintain the water pressure for a functioning drainage channel (W. Kamb et al., 1985; W. B. Kamb, 1987). As seen in Figure 9(b), for all choices of χ, the steepest (and negative) hydraulic gradients are modeled near the leading edge of the reservoir area bulges, particularly at km-100 and km-120. We see that the growing reservoir area at km-97 (RA-97), with a leading edge around km-100, causes a steeper hydraulic gradient to develop near the leading edge while the gradient gets less steep at the km-119 reservoir area where the shape of the leading edge remains relatively constant. The initial surge was observed to trigger near km-97 to km-100 in the latest surge Burgess et al. (2013), and for the purposes of this paper we trigger the surge simulation at this location after the 20 year quiescent evolution.

For future simulations that run over the course of an entire surge cycle, we can adopt a deterministic surge initiation criterion based on our quiescent-phase hydropotential results (Section 4.2) by setting a threshold on the amount of subglacial water storage up-glacier of an increasingly steep hydraulic gradient. For example, we can track the relative water build-up around the reservoir areas by calculating the area of the hydraulic gradient above zero (see Fig. 9). Once this value reaches a set threshold value, e.g., the end-of-quiescent value given by the blue line in Figure 9(b)), the flow regime is allowed to change suddenly at that location by switching from the quiescent phase friction representation (Eqn. 10) to the surge phase friction representation (Eqn. 11). This forms a unified friction law for the BBGS that can automatically initiate a surge wave. Alternatively, instead of a purely deterministic surge initiation criterion, a probabilistic method can be adopted whose density function is based on the modeled hydraulic gradient.

5.2 Surge Simulations

In this section, we present the initial surge phase modeling results with respect to velocity, basal shear stress, elevation change and hydropotential. This experiment models only the surge progressing through the mid to lower Bering Glacier trunk and corresponds roughly to the 2008-2010 portion of the latest BBGS surge. We simulate the surge by imposing the surge wave friction representation described in Section 3.3.2.2. Based on observations of the surge wave during the latest surge by Turrin et al. (2013), we set the surge wave propagation speed to $u_{front} = 50$ m/day (18.25 km/year) and as mentioned in the previous section, we set the along-flowline surge initiation location to $x_{init} = 100\ km$, i.e., at the leading edge of RA-97.

We use 132 5-day time steps (660 total simulation days) and do not include SMB forcing due to the short length of the experiment. The 5-day temporal resolution, while chosen based on computational resource considerations, is considered sufficient to capture the rapid dynamic changes that occur during a surge. We choose not to enforce SMB as its effect would be less than 5 m elevation change throughout the simulation, based on Equation 2.4, and we are more interested in an experiment that isolates the larger dynamic component of the surge. A simulation that included SMB-forcing would not give results that are significantly different than those presented in this section.

5.2.1 Velocity

Figure 12 displays the surface velocity at various times during the simulated initial surge phase. Near the beginning of the simulation (Figure 12(a)), when the surge has only affected a portion of the glacier (from km-100 to km-110), large surface velocities exceeding 1800 m/year ($\sim$5 m/day) are identified. The fastest speeds at this time reach 10.25 m/day which is similar to maximum observed velocities in this area given by Burgess et al. (2013) of 9 m/day. At later time steps, when the surge is progressing down-glacier, velocities subside in this area. When the surge front is moving through the thick ice along km-110 to km-120 (Fig. 12 (c)), modeled ice-surface velocities are noticeably reduced and do not exceed 1000 m/year aside from isolated regions near the margins that may have arisen due to edge effects in the model. This area of thick ice contained relatively few surge crevasses compared to the rest of Bering's trunk (Trantow & Herzfeld, 2018), which is consistent with the lower velocities modeled here.

We observe similar spatial velocity patterns in Bering's trunk between our modeled velocities and the maps produced by Burgess et al. (2013) for 2010. Burgess et al.

(2013) labels the areas of high velocity in Central Bering as "surge fronts", however, our model shows that these spatial patterns are persistent across the initial surge phase. The assumed surge fronts in Figure 3 of Burgess et al. (2013) are transposed on our modeled velocity map using black lines in Figure 12(b). Our results indicate that these high-velocity areas in Central Bering are not associated with surge fronts but are rather attributed to particulars of the local bedrock topography where the spurs act like a nozzle through which ice moves faster relative to the incoming ice up-glacier.

In addition, Burgess et al. (2013) observed that the surge appeared to subside between the initial acceleration in 2008 (initial surge phase) and the reinitiation in 2011 (second surge phase). Our simulation here, however, shows that while the surge kinematic wave continues to progress down glacier, peak ice-surface speeds lessen when propagating through the ice between km-110 and km-125. This resembles an apparent subsidence in surge activity but in fact the surge continues to progress uninterrupted as the wave propagates down-glacier. Not only does the glacier become wider after km-110, but the subglacial spurs are not as prominent and do not reach as far toward the center of the glacier compared to those found in Upper Bering (Figure 10(a)). Hence, there is less of a nozzle-effect as the surging ice is allowed to flow more easily down-glacier (longitudinally), across a greater width of the glacier, without being blocked by the spurs. Therefore, relative to the rest of Bering's trunk, less stress is experienced at the ice-surface at this location resulting in fewer surge crevasses as reflected by observations and modeling in Trantow and Herzfeld (2018).

Near the end of the simulation (Figure 12(d)), when the surge front has reached km-125, peak modeled velocities begin to once again increase, reaching maximums near 10 m/day (excluding modeled velocities in the overflow area, which are unrealistically high based on previous observations (Trantow, 2020) likely due to edge effects). Here, the subglacial spurs emanating from the Khitrov Hills in the north and the Grindle Hills in the south become more prominent increasing the nozzle-effect. Moreover, the anomalous rise of bedrock topography in the central trough, circled in red at km-125 in Figure 10(a), adds to the nozzle-effect effectively creating two "nozzles" together with the spurs on either side.The modeled peak velocities in this area are consistent with those derived from the velocity map presented in Trantow and Herzfeld (2018) and in Section 5.3. The simulation ends as the surge wave reaches the final reservoir area near km-128 approximately 2 years after surge initiation.

5.2.2 Basal Shear Stress

Figure 13 gives the modeled basal shear stress in the x-direction at the same time stamps in Figure 12. The x-direction is coincident with the along-flow direction for Central Bering where the surge is occurring in this simulation. The figure views Bering Glacier from the bottom with the surge wave propagating down-glacier from left to right. The surge front is clearly marked in each subfigure as a dividing line between low basal shear stresses up-glacier (white/yellow) and high basal shear stresses down-glacier (orange/red) of the surge front. This figure reveals that basal shear stresses are reduced far up-glacier, well above the initiation location at km-100, where quiescent basal friction parameterization still applies. This result reflects observations of a surge wave that propagates down-glacier while also having effects up-glacier in regions not (yet) actively surging, e.g., the formation of en-échelon crevasses (Figure 3(f)) (Herzfeld & Mayer, 1997; Herzfeld et al., 2004; Herzfeld, McDonald, Stachura, et al., 2013).

5.2.3 Elevation Change

Figure 14 shows elevation change throughout the surge simulation. Elevation-change is analyzed starting with time-step 32 to allow sufficient time for the initial surface to

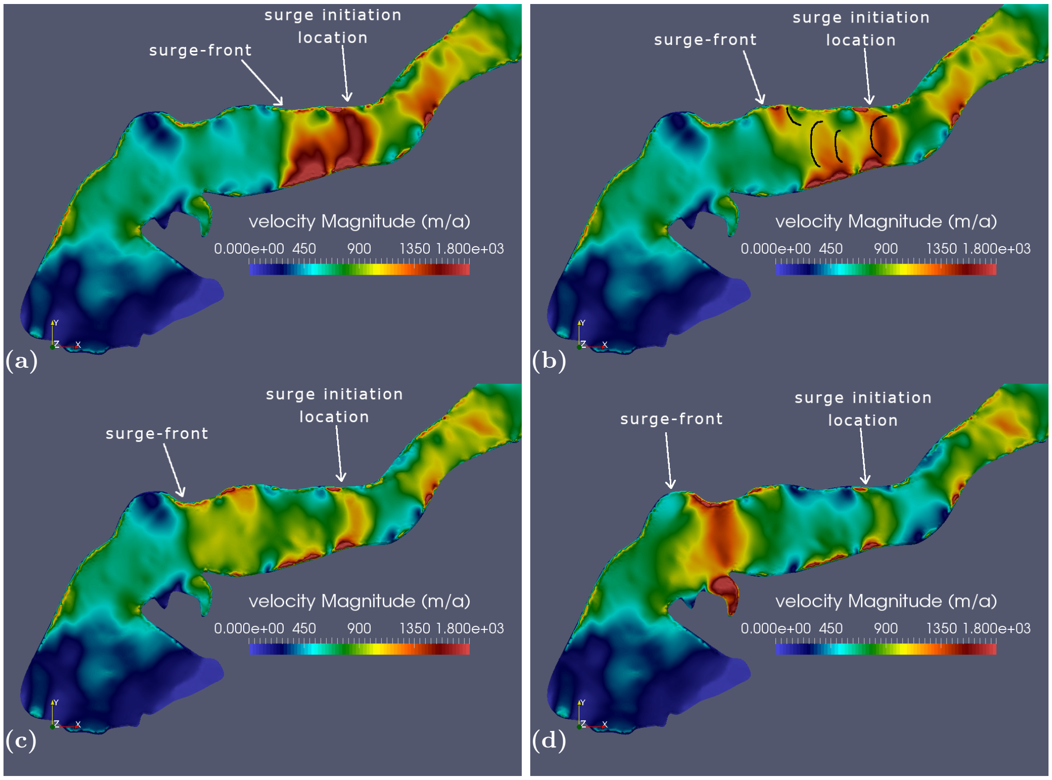

Figure 12. Modeled surface velocity throughout the initial surge phase simulation. Velocity given in meters per year. Arrows indicate the surge initiation location and the approximate location of the surge front for each time step, which bound the active surging area (activation zone). (a) Velocity at time step 10, (b) velocity at time step 40 with the "surge fronts" assumed by Burgess et al. (2013) marked in black, (c) velocity at time step 80 and (d) velocity at time step 132.

adjust to, or "relax" from, the stress inconsistencies between the input surface DEM and the other fixed geometrical boundaries at the bed and margins (Trantow & Herzfeld, 2018).

Subfigure 14(a) shows the overall mass transfer near the beginning of the surge simulation to the end. In general, we see mass transfer from the upper trunk to the lower trunk, that is, from the areas affected by the surge to the down-glacier areas not yet affected (in terms of basal friction). We see elevation changes that exceed 50, and even 100 m, over the course of approximately 1 year, which is consistent with altimetric observations (Herzfeld, McDonald, Stachura, et al., 2013; Burgess et al., 2013; Trantow & Herzfeld, 2016).

Subfigure 14(b) shows the elevation change from time step 32 to time step 80, i.e. the first ≈250 days of the initial surge phase after the relaxation period, which shows that surface lowering in the activation zone (≈3.9-4.0 $\times 10^5$ UTM-East) is larger than at the end of the surge simulation when ice from further up-glacier flows into the evacuated region. During this time period mass has begun to transfer from reservoir area RA-97 down-glacier to the receiving areas in lower Central Bering around ≈3.8-3.9 $\times 10^5$ UTM-East. Notably, we see significant elevation changes far down glacier of the active region indicating that regions away from the active surge zones are affected by the increased flow speeds long before the surge front reaches that area.

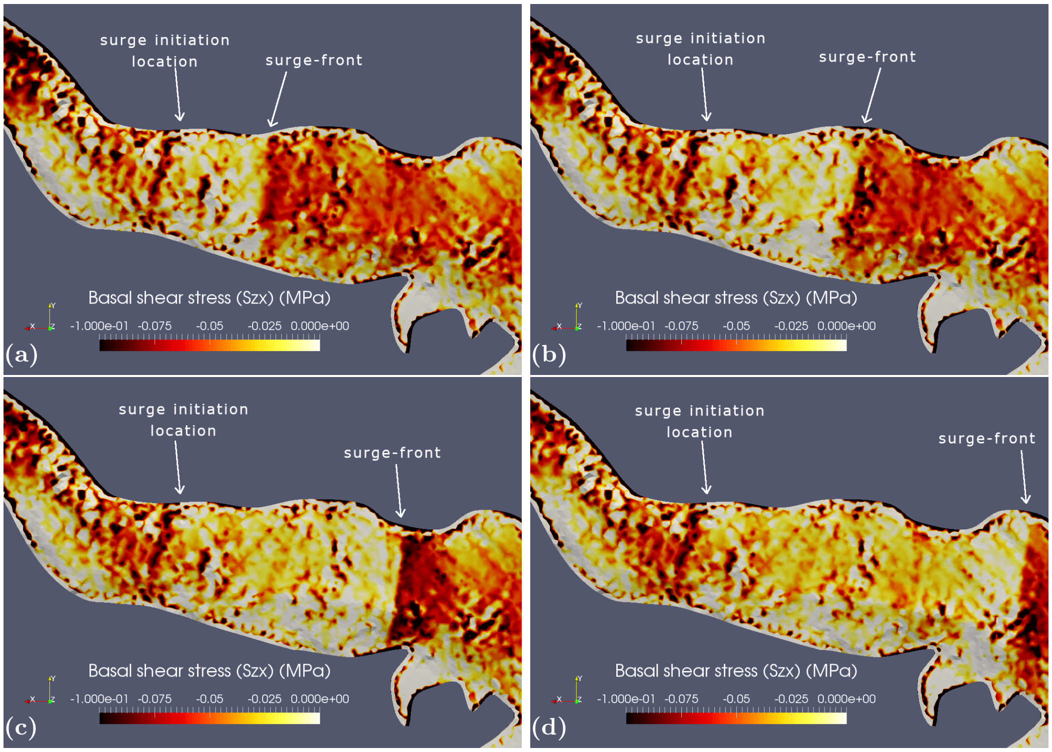

Figure 13. Modeled basal shear stress throughout the initial surge phase simulation. Displayed is the basal shear stress that acts on the plane orthogonal to the z-axis in the direction of the x-axis. Arrows indicate the surge initiation location and the approximate location of the surge front for each time step. Note that we are viewing the glacier from the bottom, with the positive x-axis pointing to the left, unlike the other figures in this section where the glacier is viewed from above with the positive x-axis pointing to the right. Stress is given in units of mega-Pascals. (a) Basal shear stress at time step 10, (b) basal shear stress at time step 40, (c) basal shear stress at time step 80 and (d) basal shear stress at time step 132.

Finally, subfigure 14(c) illustrates the elevation change from time step 80 to time step 132, which corresponds to the last 250 days of our initial-phase surge simulation. This figure shows that surface lowering only occurs in the down-glacier half of the activation zone ($\approx$ 3.75-3.95 $\times 10^5$ UTM-East) where surge speeds are the largest (see Figure 12(c) and (d)). The mass transfer to Upper Bering comes from the lower Bagley Ice Field, across the BBJ, which relieves the quiescent phase mass-build up of that area (RA-64). At each moment in time the location of the surge front is obvious when looking at temporally-local elevation changes where the surface is actively lowering behind the surge front and raising ahead of it, which resembles the often identified “surge bulge”. The elevation pattern near the end of the simulation is consistent with observations derived from CryoSat-2 data as described in Trantow and Herzfeld (2016).

5.2.4 Hydropotential

Finally, we take a look at the changing hydropotential and hydropotential gradient along-flowline during the surge simulation in a way similar to the quiescent analysis carried out in Section 4.2 and Figure 9 (sans plots of relative surface-change). Figure 15 shows these quantities near the beginning of the surge (after time step 32, a half-

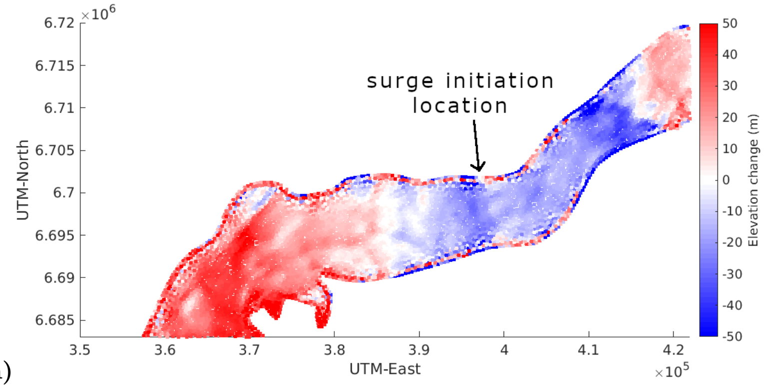

(a)

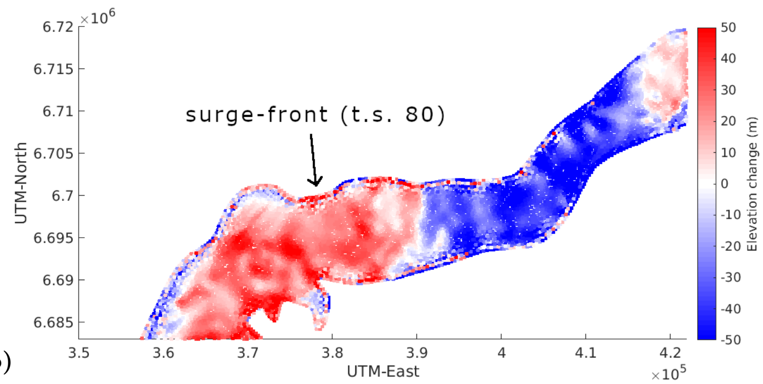

(b)

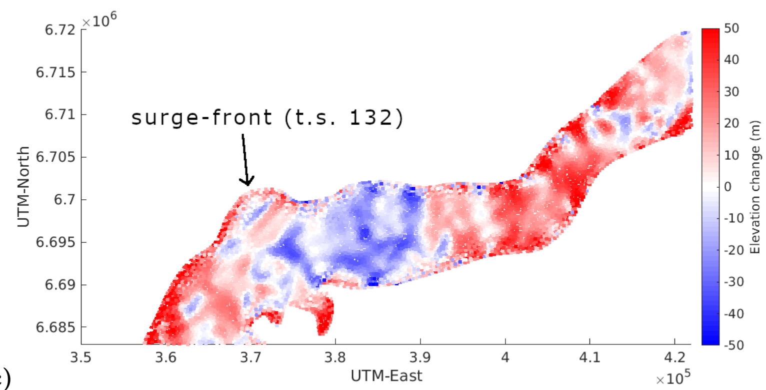

(c)

Figure 14. Modeled elevation change throughout the initial surge phase simulation. Areas of blue indicate a surface lowering while areas of red indicate surface-elevation gain. (a) Elevation difference between time 32 and time 132 showing an overall mass transfer from Upper Bering to Lower Bering. The black arrow indicates the surge initiation location at along-track km-100. (b) Elevation difference between time 32 and time 80 with major surface lowering both above and below the surge initiation location and surface gains below 3.9 $\times 10^5$ UTM-East. Ice-mass has started to transfer from RA-97 to receiving areas down-glacier. The black arrow marks the approximate surge front at time-step 80 that bounds the activation zone together with the surge initiation location. (c) Elevation difference between time 80 and time 132 showing surface lowering between 3.75 and 3.9 $\times 10^5$ UTM-East and surface-elevation gains in the previously-lowered Upper Bering due to mass transfer from RA-64 in Bagley Ice Field. The black arrow marks the approximate surge front location at time-step 132.

year into the initial surge phase) and in the middle of the initial surge phase after the surge front has progressed 20 km down-glacier (time step 80 or Day-400 of the initial surge phase). The first aspect to note is the change in hydropotential in the surge activation zone (km-100 to km-120). The hydraulic gradient has decreased throughout most of the activation zone implying that the passing surge wave, and the fast-sliding activation zone behind it, serves to further degrade the efficiency of the basal drainage system.

Previous theories predict that the passing of the surge kinematic wave would activate the switch from an EDS to an IDS (W. B. Kamb, 1987). However, we show here, and in the previous section, that the basal drainage system becomes less efficient throughout quiescence and becomes even more inefficient once the surge wave passes through. Our approach also does not require any assumption of a linked-cavity system, or of any specific bed-type in general. We also see that the small ($\sim$3 km) region centered at km-103 of positive hydraulic gradient, where water is predicted to collect, has shifted slightly down-glacier (indicated by an arrow in Figure 15(b)). This results implies that water accumulation areas may shift during the progression of the surge in areas up-glacier form the surge front.

We also note that in the region up-glacier of the initiation location, the hydropotential levels out from time-step 32 to time-step 80 with less variation along-flowline and a reduction in the estimated amount of basal water collection. This observation indicates that regions far up-glacier of the activation zone, which are modeled using the normal flow friction law value β_q, are becoming more efficient in their basal drainage indicating a return to a quiescent state as mass is redistributed down-glacier during the surge.

5.3 Second Surge Phase Analysis Based on Satellite Observations

While numerical experiments were only carried out for the first surge phase in this paper, for completeness we investigate the second surge phase with respect to velocity and hydropotential using satellite observations. Elevation-change analysis for the second phase of the last BBGS surge is described in Trantow and Herzfeld (2016) and diagnostic modeling for the initial part of the second-phase in early 2011 is reported in Trantow and Herzfeld (2018) where insights into the stress regime are provided.

In this section, we use CryoSat-2 DEMs to derive observation-based hydropotential maps of the BBGS during the 2011-2013 phase of the latest surge in order to infer drainage characteristics throughout the glacier during the peak of the surge in early 2011 (March-April), when glacier velocities exceeded 22 m/day (Figure 16 (a)), and near the end of the surge in 2013 when dynamic activity in Bering Glacier had reduced significantly (Figure 16 (b)), with velocities below 2 m/day in most of Lower and Central Bering. These velocity maps are derived using ImGRAFT feature-tracking methods applied to Landsat-7 and Landsat-8 imagery respectively (see Section 2.2).

As seen in the early 2011 map (Figure 16 (a)), reliable velocity estimates are difficult to attain while the glacier is surging, with features used in correlation rapidly deforming over the course of several days (Trantow & Herzfeld, 2018). Moreover, the stripping in Landsat-7 imagery (Markham et al., 2004) greatly reduces the area for which ice-velocities can be derived. For 2013, we are able to obtain more accurate overall velocity estimates for the BBGS (Figure 16 (b)), because 2013 Landsat-8 imagery is of higher quality than 2011 Landsat-7 imagery and because the glacier flowed much slower in 2013 than in 2011. We note however, that the Sentinel-1 SAR imagery, available beginning in 2014, provide the most reliable and comprehensive velocity estimates (e.g., Figure 11(a)) due to the fact that SAR imagery is not complicated by the presence of clouds.

CryoSat-2 began providing reliable glacier height measurements around the start of the second phase of the most recent BBGS surge. As shown in Trantow and Herzfeld (2016), we can derive ice surface DEMs, and thus unique hydropotential maps, every six

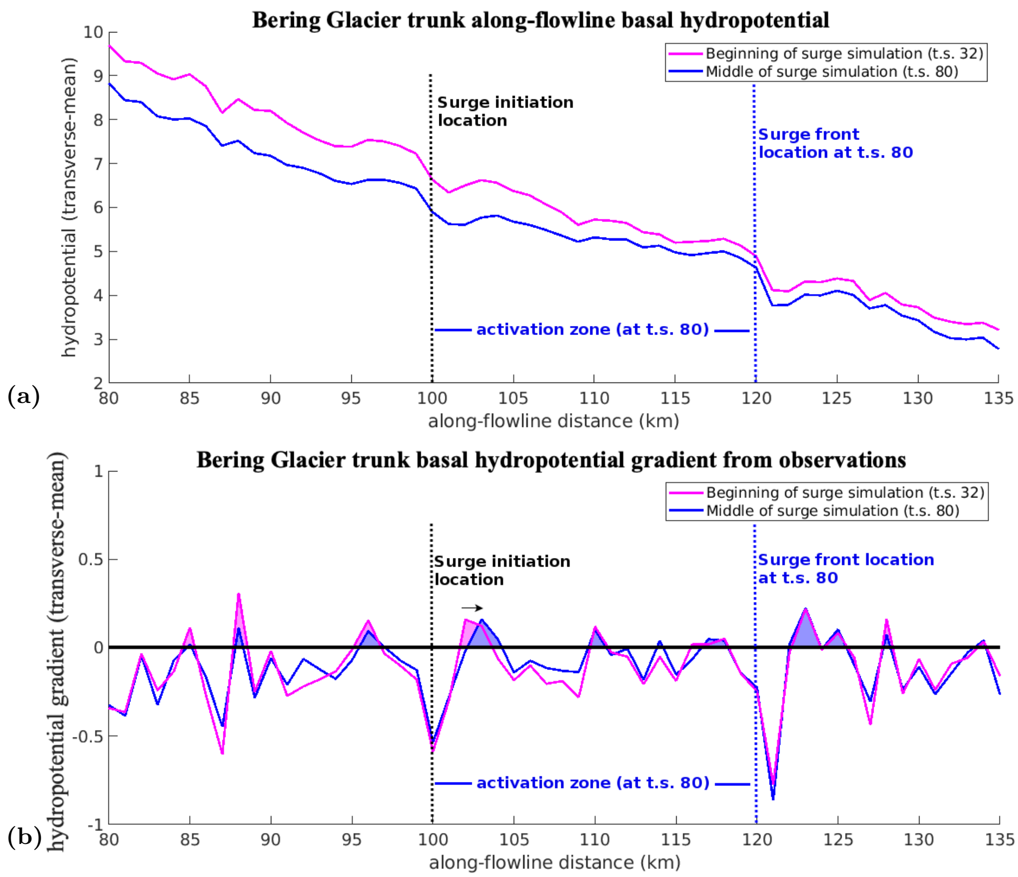

Figure 15. Hydropotential and hydraulic gradient during the initial surge phase simulation. The magenta curves correspond to the glacier state near the beginning of the surge at time step 32 (Day-160) and the blue lines correspond to the glacier state after the surge wave has propagated 20 km down-glacier at time step 80 (Day-400). Labeled are the surge initiation location along-flowline (black dotted line) and the surge front location along-flowline at time step 80 (blue dashed line). Areas with positive gradients are shaded indicating estimated water storage locations. (a) Modeled hydropotential (MPa) and (b) modeled hydraulic gradient ($\frac{MPa}{km}$). The small black arrow indicates the shift of a water accumulation zone down-glacier during the surge.

months from the CryoSat-2 data. Therefore, we can estimate hydropotential based on CryoSat-2 surface elevation observations rather than from modeled BBGS surface heights.

Our CryoSat-2-based hydropotential analysis for the second phase of the surge (2011-2013) assumes zero effective pressure ($\chi = 1$). By 2011, the surge has passed through most of Bering's trunk with the front advancing to km-124 where the large reservoir area (RA-124) was observed in 2011 (Herzfeld, McDonald, Stachura, et al., 2013).

Figures 16(c) and (d) compare the CryoSat-2-estimated basal hydropotential for Summer 2011 (May 2011-October 2011) during the main acceleration phase and Summer 2013 (May 2013-October 2013) once most of the major surge activity in Bering Glacier had ceased. In Summer 2013, the hydropotential begins to conform more to the bed topographical potential and becomes less dominated by ice overburden pressure, with less water dispersing transversely and increased water drainage efficiency occurring down-glacier. Looking at Bering Glacier's trunk, we see the contour lines become more evenly spaced and more transversely aligned in 2013. This indicates that a more steady, down-glacier flow, i.e. efficient flow, has manifested after the surge had ended by 2013 (in Central Bering Glacier). We also see a reduction in the amount of hydropotential wells throughout the trunk indicating less capacity to store water beneath the glacier by the end of the surge.

Similar to Figure 15, we plot the along-flowline hydropotential and hydropotential gradient derived from the CryoSat-2 data for Summer 2011 (green lines) and Summer 2013 (orange lines) in Figure 17. The hydropotential profiles in Figure 17(a) above km-124, i.e. where the surge front is in 2011, are smoother than those predicted by the model both before and during the surge, which is expected based on the redistribution of mass caused by the passing surge that transferred mass from reservoir areas to receiving areas. With $\chi = 1$, thickness still contributes significantly to the hydropotential calculation, and after the surge passes through the trunk, thickness is more evenly distributed. Furthermore, by the end of the surge phase in Summer 2013 (orange line) we see that the hydropotential throughout the entire trunk becomes even smoother than in Summer 2011 (green line).

Figure 17(b) plots the hydropotential gradient for Summer 2011 (green) and Summer 2013 (orange). In Summer 2011, we see that above the surge front at km-124, the gradient is below zero everywhere indicating down-glacier drainage and a destruction of the glacier's hydrologic storage areas identified in the quiescent analysis. The gradient variability remains high however, indicating that the glacier has not yet transitioned to a more uniform and efficient drainage state above the surge front. At km-124, we see that there remains an area with a positive gradient, i.e. a water storage area which will soon be released during the second surge phase.

By Summer 2013, essentially no areas of water storage remain throughout Bering's trunk. Furthermore, the gradient variability has reduced from its Summer 2011 state, which indicates more uniform flow through the trunk.

5.4 Transition Back to Quiescence

In theory, after redistribution of mass throughout the glacier system, the glacier returns once more to a stable geometry. Slowdowns in the Alaskan-type surge-glacier systems are usually correlated with large outburst floods at the glacier terminus (W. Kamb et al., 1985), and the subglacial drainage system returns to an efficient one. This transition typically begins at the front of the glacier and slowly moves up-glacier until the entire glacier system returns to an EDS.

This process is reflected by observed velocity at the cessation of the surge. The derived velocity map in Figure 16(b) from 2013 shows that low velocities (less that 1 m/day) exist in Lower Bering while higher velocities (2-5 m/day) remain in Upper Bering and the Bagley Ice Field. From 2012 onwards, the region of fast flow shrinks to only the Bagley Ice Field, with peak velocities also decreasing (Trantow, 2020). The highest velocities in 2013 remain in the Bagley Ice Field and just below the Bering-Bagley junction where basal slopes are high. By the year 2016, the entire glacier system is moving at less than 1 m/day, and effects of the recent surge have disappeared entirely, with the whole system in a state of low basal pressures and efficient drainage (Figure 11(a)).

The hydropotential results of the second surge phase from CryoSat-2 observations suggest that the mass redistribution occurring during the surge leads to more efficient drainage with less hydropotential wells and more longitudinally-oriented flow down-glacier. However, to model surge arrest properly the model would need to account for the relief in basal water pressure that begins at the glacier terminus and propagates up-glacier, as reflected in the velocity observations. This effect can be achieved by using a friction law similar to the surge-phase representation (Equation 11) but would now propagate

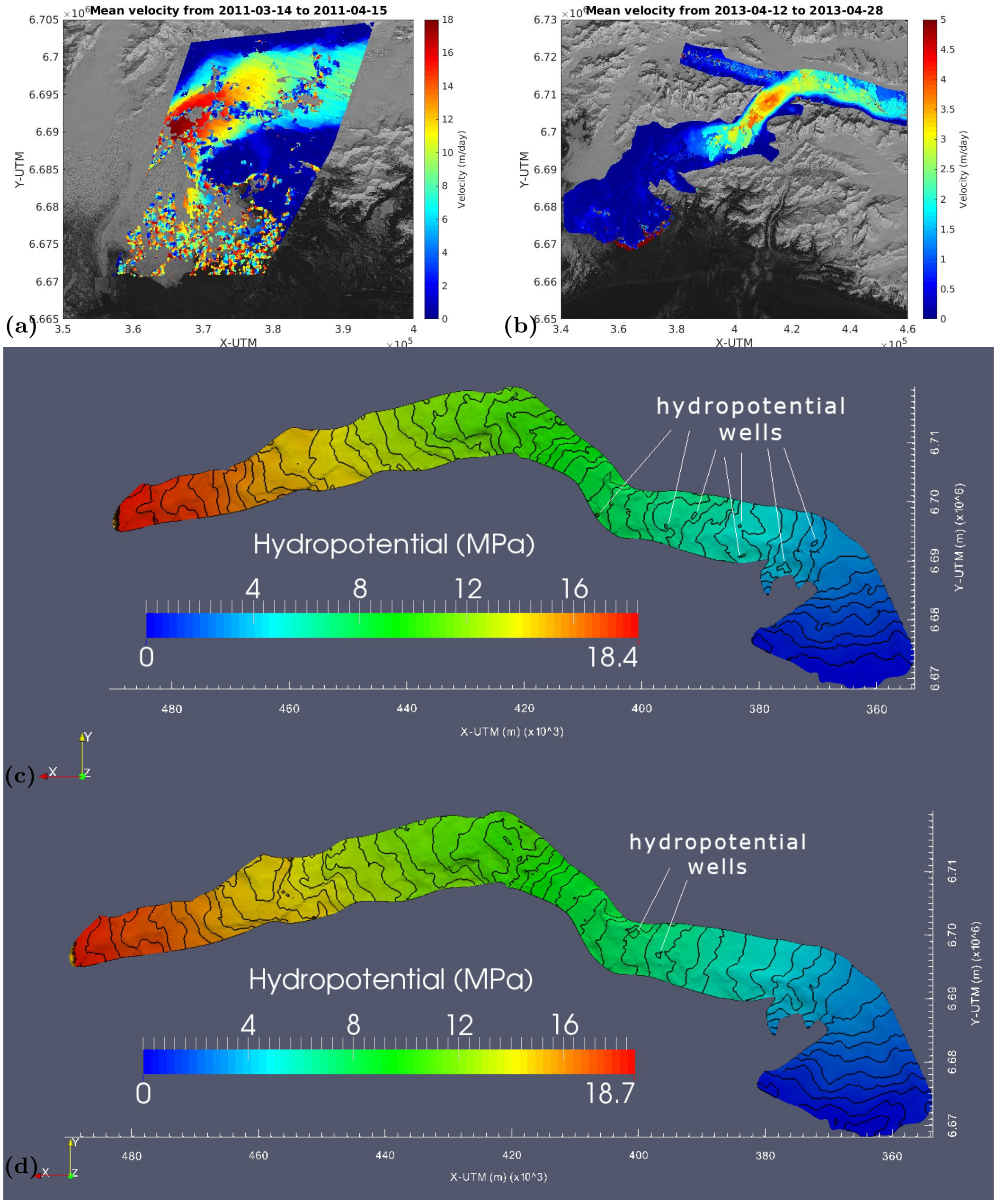

Figure 16. Velocity and basal hydropotential derived from observations during and after the second surge phase in Bering Glacier. (a) Mean ice-surface velocity between 2011-03-14 and 2011-04-15 derived from Landsat-7 imagery. (b) Mean ice-surface velocity between 2013-04-12 and 2013-04-28 derived from Landsat-8 imagery. (c) Hydropotential derived from the ESA CryoSat-2 Baseline-C DEM for Summer 2011 (May 2011 - October 2011). (d) Hydropotential derived from the ESA CryoSat-2 Baseline-C DEM for Summer 2013 (May 2013 - October 2013). Basal hydropotential wells are indicated via white lines. Both maps use the JPL-WISE bed topography maps in their estimation of hydropotential. Note that subfigures (c) and (d) look at the base of the BBGS, with the positive x-direction pointing to the left and ice flow down-glacier moving from left to right.

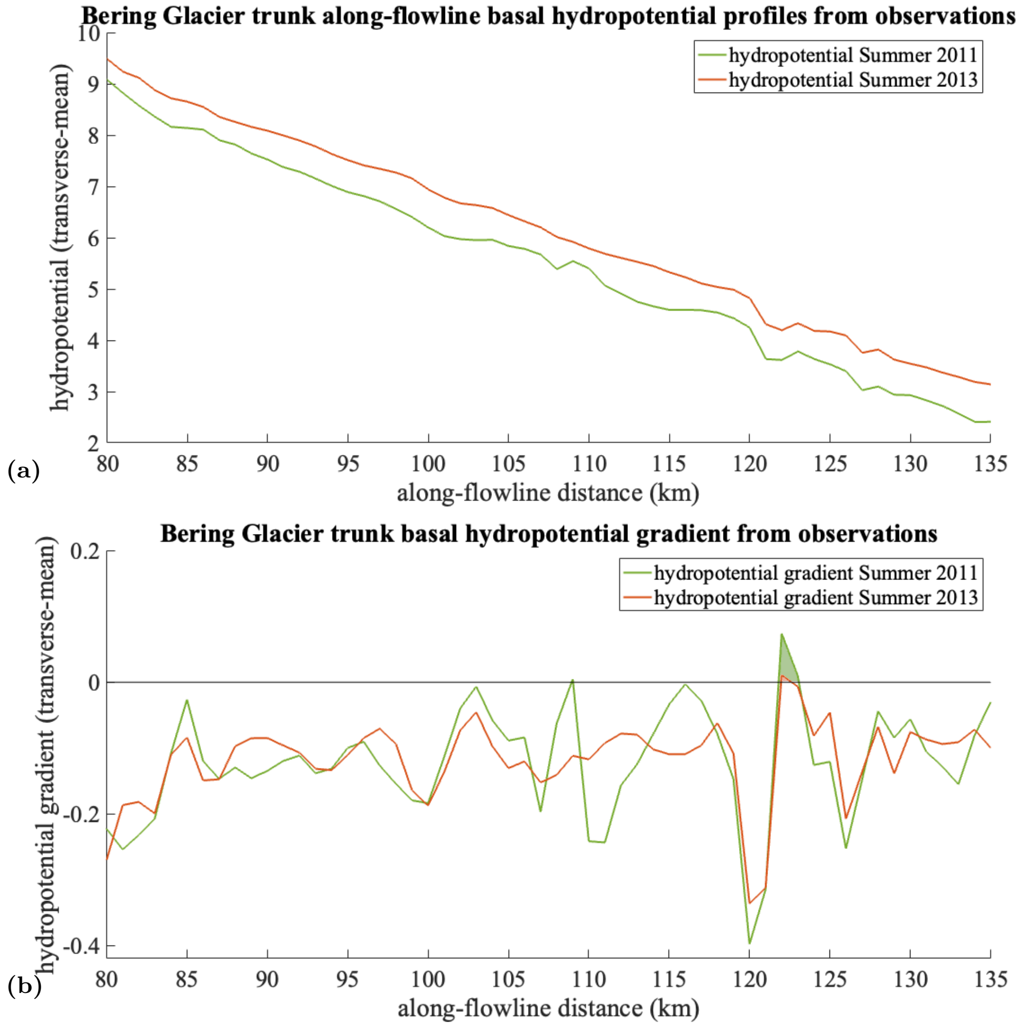

Figure 17. Hydropotential and hydraulic gradient from observations of the second phase of the surge. The green curves are derived from the CryoSat-2 surface DEM for Summer 2011 (May 2011 to October 2011) during the second phase of the surge, while the orange curves are from the corresponding DEM for Summer 2013 (May 2013 to October 2013) near the end of the surge phase. CryoSat-2 DEMs from Trantow and Herzfeld (2016). (a) Hydropotential (MPa) and (b) hydraulic gradient ($\frac{MPa}{km}$). Areas with positive gradients are shaded indicating water storage locations.

up-glacier, increasing the basal friction coefficient, β, as it passes. Implementation of such a law to model the transition back to quiescence is left for future BBGS modeling experiments.

6 Summary and Conclusions

In this paper, we utilized numerical simulations, supplemented by satellite and airborne observations, to investigate dynamic, geometric and hydrologic aspects of both the quiescent and surge phases of the Bering-Bagley Glacier System, Alaska. The analysis centers on inter-annual changes of mass redistribution throughout the glacier system and its implications on water drainage. The latter is achieved through calculation of hydropotential, which is bounded by a range of realistic basal water pressures. Unique to our approach is the utilization and synthesis of widely available observational data and simply-parameterized ice-dynamic modeling, which can be applied to other studies of large and complex glacier systems.

The quiescent phase simulation shows a steepening of local geometry in several identified reservoir areas, retainment of water and slowed-drainage paths that build throughout Bering Glacier's trunk leading to prime surging conditions. These results are mostly attributed to the particular properties of the bedrock topography. The most significant features are a series of subglacial ridges, which are extensions of the surrounding mountains beneath the glacier. These subglacial ridges lead to damming of ice and water over the course of quiescence. The build-up of ice at the subglacial ridges forms reservoir areas that slow down-glacier drainage in the areas directly up-glacier and can even lead to water retainment in the closest 2-4 km at several locations (specified in Figures 9 and 10). The simulation of the quiescent phase shows an increase of stored water in Bering Glacier's trunk by a factor of 2.46 over 20 years of evolution, which is estimated by calculating the positive hydraulic gradient area (shaded regions in Fig 9).

Moreover, the changing geometry during quiescence slows the overall down-glacier drainage through Bering Glacier's trunk through increased transverse water paths caused by the various ice dams. The difference in hydropotential across Bering's trunk, from km-80 to km-135, decreased between 10.4% and 16.6% after 20 years of quiescent flow. The increasing amount of stored water and slowed down-glacier drainage lead to ever-more water in the subglacial drainage system at a given time which would allow the glacier to better sustain an inefficient drainage system and high-water pressures as the quiescent phase matures. While surge and quiescent phases are modeled in separate simulations, we propose a surge initiation criterion that is based on the inferred amount of stored water based on the hydropotential calculation. The surge initiation location at RA-97 is suggested by both our model and by observations of the latest surge.

Based on an observed surge wave in the BBGS, we propose a surge wave friction representation to simulate the initial surge phase through Bering Glacier's main trunk. This spatiotemporally-variable friction representation mimics a propagating surge wave, initiated at some trigger location, that activates fast-moving ice by scaling the linear basal friction parameter as it passes. Modeled velocities were consistent with those observed during the early stages of the latest surge in the BBGS from 2008 through 2010. Our results show that while changes in basal conditions are initially concentrated within an activation zone, as prescribed by the evolving friction function, significant basal shear stress and elevation changes occur throughout the glacier system, even outside of the areas of actively surging ice, which has been observed, for example, through the presence of en-échelon far up-glacier in the Bagley Ice Field.

Locations where flow velocities are highest in the active surging area are due to a nozzle-like effect where fast-flowing ice is squeezed through the center of the glacier between the subglacial ridges. Notably, these regions are stationary throughout the surge phase and do not correspond to surge fronts as suggested by Burgess et al. (2013). Furthermore, we show that while surge activity appears to subside near the end of the initial surge phase, e.g. in 2010 of the latest surge Burgess et al. (2013), the surge kinematic wave actually continues to progress uninterrupted through a portion Bering's trunk that is wide and has very few subglacial spurs. This result further highlights the control of glacier geometry, particularly bedrock topography, on the progression and expression of a BBGS surge.

As the simulated surge front moves down-glacier, we find that the drainage efficiency further decreases within the active surging area. Glacier geometry begins to level out after ice in the reservoir areas is transferred to the receiving areas. Analysis of hydropotential maps, derived from CryoSat-2 altimeter data, indicates that the drainage system of the BBGS shows characteristics of a return to an efficient drainage system, where down-glacier flow dominates and hydropotential wells disappear.

Our results indicate that other studies aiming to understand surging and dynamic peculiarities of large complex glacier systems should prioritize attaining quality bedrock topography maps. While our hydropotential approach does not model the subglacial drainage system explicitly, it still provides valuable information on the pattern of hydrologic drainage which can be used to inform more complex representations for modeling basal friction during glacier surges. Since our hydropotential estimates rely only on geometric observations, a quality time series of surface DEMs derived from satellite altimetry, e.g. CryoSat-2 or ICESat-2 measurements, can be sufficient to investigate the evolution of key glacial drainage characteristics without the difficulty of attaining comprehensive hydrologic data. Moreover, hydropotential maps derived from observations can be used in comparison to those generated by a numerical model in order to better constrain important parameters such as the friction coefficient.

In summary, we provide a full picture of an entire BBGS surge cycle using a numerical model and satellite observations, with our model capturing key characteristics of the surge cycle including peak velocities, building reservoir areas and mass transfer. The bedrock topography DEM is an important component of the model's ability to capture observed spatial qualities of the glacier dynamics such as locations of reservoir areas and velocity patterns. This paper improves physical process understanding of a glacier surge and provides a modeling approach that simulates only ice-dynamics and mass transfer, which in turn are used to infer characteristics of subglacial water drainage. In future studies, we hope that access to better computing resources will allow higher spatiotemporal resolution, longer simulations and increased model complexity such as the addition of explicit hydrologic modeling that is coupled with the glacier dynamics allowing a unified friction law.

7 Open Research

The Solver Input Files (SIF) for the Elmer/Ice simulations performed in this analysis, along with the Bering Glacier specific datasets and User Functions (USF), are available in TT's GitHub repository:
`https://github.com/trantow/bbgs_elmer`.

Sentinel-1 SAR data are freely available at the Copernicus Open Access Hub:
`https://scihub.copernicus.eu/`

The Sentinel Application Platform (SNAP) (Veci et al., 2014), used in this project to derive velocity maps, is also freely available for download at:
`https://step.esa.int/main/download/snap-download/`

Acknowledgments

We would like to thank Dr. Ralf Greve (Institute of Low Temperature Science, Hokkaido University, Sapporo, Japan) for his invaluable input in our understanding of ice-dynamic modeling and for co-advising the first author in the research pertaining to this paper. We thank Eric Rignot (Jet Propulsion Laboratory, Pasadena, USA and University California Irvine, USA) and Jeremie Mouginot (University California Irvine, USA) for sharing their bed topographic data of the BBGS and Veit Helm (Alfred Wegener Institute, Bremen, Germany) for sharing their CryoSat-2 TFMRA-swath data for the BBGS. Support of this research through the U.S. National Science Foundation's Office of Polar Programs (Awards OPP-1745705 and OPP-1942356), Office of Advanced Cyberinfrastructure (Award OAC-1835256), Arctic Natural Sciences Program (Award ARC-1148800) and Geography and Spatial Sciences (Award GSS-1553133), and through NASA Cryospheric

Sciences (Award NNX17AG75G) is gratefully acknowledged (U. C. Herzfeld is the PI of all awards).

References

Andrews, L. C., Catania, G. A., Hoffman, M. J., Gulley, J. D., Lüthi, M. P., Ryser, C., et al. (2014). Direct observations of evolving subglacial drainage beneath the greenland ice sheet. *Nature*, *514*(7520), 80–83.

Arcone, S. A. (2002). Airborne-radar stratigraphy and electrical structure of temperate firn: Bagley ice field, alaska, usa. *Journal of Glaciology*, *48*(161), 317–334.

Aschwanden, A., Fahnestock, M. A., Truffer, M., Brinkerhoff, D. J., Hock, R., Khroulev, C., et al. (2019). Contribution of the greenland ice sheet to sea level over the next millennium. *Science advances*, *5*(6), eaav9396.

Benn, D., Fowler, A. C., Hewitt, I., & Sevestre, H. (2019). A general theory of glacier surges. *Journal of Glaciology*, *65*(253), 701–716.

Bindschadler, R. (1983). The importance of pressurized subglacial water in separation and sliding at the glacier bed. *Journal of Glaciology*, *29*(101), 3–19.

Björnsson, H. (1974). *Explanations of jökulhlaups from Grímsvötn, Vatnajökull, Iceland.*

Björnsson, H. (1998). Hydrological characteristics of the drainage system beneath a surging glacier. *Nature*, *395*(6704), 771.

Bouffard, J. (2015). CRYOSAT-2: Level 2 product evolutions and quality improvements in Baseline C (v3).

Boulton, G., Lunn, R., Vidstrand, P., & Zatsepin, S. (2007). Subglacial drainage by groundwater-channel coupling, and the origin of esker systems: part 1-glaciological observations. *Quaternary Science Reviews*, *26*(7-8), 1067–1090.

Brinkerhoff, D. J., Meyer, C. R., Bueler, E., Truffer, M., & Bartholomaus, T. C. (2016). Inversion of a glacier hydrology model. *Annals of Glaciology*, *57*(72), 84–95.

Burgess, E. W., Forster, R. R., Larsen, C. F., & Braun, M. (2013). Surge Dynamics on Bering Glacier, Alaska, in 2008–2011. *The Cryosphere*, *6*, 1251–1262.

Choi, Y., Morlighem, M., Rignot, E., & Wood, M. (2021). Ice dynamics will remain a primary driver of greenland ice sheet mass loss over the next century. *Communications Earth & Environment*, *2*(1), 1–9.

Chu, W., Schroeder, D. M., Seroussi, H., Creyts, T. T., Palmer, S. J., & Bell, R. E. (2016). Extensive winter subglacial water storage beneath the Greenland Ice Sheet. *Geophysical Research Letters*, *43*(24), 12–484.

Clarke, G. K., Collins, S. G., & Thompson, D. E. (1984). Flow, thermal structure, and subglacial conditions of a surge-type glacier. *Canadian Journal of Earth Sciences*, *21*(2), 232–240.

Cuffey, K., & Paterson, W. S. B. (2010). *The Physics of Glaciers* (4th ed.). Elsevier.

Dowdeswell, J. A., Hamilton, G. S., & Hagen, J. O. (1991). The duration of the active phase on surge-type glaciers: contrasts between svalbard and other regions. *Journal of Glaciology*, *37*(127), 388–400.

Eisen, O., Harrison, W., Echelmeyer, K., Bender, G., & J.Gorda. (2005). Variegated Glacier, Alaska, USA: A century of surges. *Journal of Glaciology*, *51*, 399-406.

Fatland, D., Lingle, C., & Truffer, M. (2003). A surface motion survey of Black Rapids Glacier, Alaska, U.S.A. *Annals of Glaciology*, *36*, 29–36.

Fatland, D. R., & Lingle, C. S. (1998). Analysis of the 1993-95 Bering Glacier (Alaska) surge using differential SAR interferometry. *Journal of Glaciology*, *44*(148), 532–546.

Fatland, D. R., & Lingle, C. S. (2002). InSAR observations of the 1993-95 Bering Glacier (Alaska, USA) surge and a surge hypothesis. *Journal of Glaciology*, *48*(162), 439–451.

Felikson, D., Bartholomaus, T. C., Catania, G. A., Korsgaard, N. J., Kjær, K. H., Morlighem, M., et al. (2017). Inland thinning on the greenland ice sheet controlled by outlet glacier geometry. *Nature Geoscience*, *10*(5), 366–369.

Fitzpatrick, A. A., Hubbard, A., Joughin, I., Quincey, D. J., Van As, D., Mikkelsen, A. P., et al. (2013). Ice flow dynamics and surface meltwater flux at a land-terminating sector of the Greenland ice sheet. *Journal of Glaciology*, *59*(216), 687–696.

Fleischer, P. J., Bailey, P. K., Natel, E. M., Muller, E. H., Cadwell, D. H., & Russell, A. (2010). The 1993-1995 surge and foreland modification, Bering Glacier, Alaska. *Geological Society of America Special Paper*(462), 193–216.

Fleurian, B. de, Werder, M. A., Beyer, S., Brinkerhoff, D. J., Delaney, I., Dow, C. F., et al. (2018). SHMIP The subglacial hydrology model intercomparison Project. *Journal of Glaciology*, *64*(248), 897–916.

Fleurian, B. d., Gagliardini, O., Zwinger, T., Durand, G., Meur, E. L., Mair, D., et al. (2014). A double continuum hydrological model for glacier applications. *The Cryosphere*, *8*(1), 137–153.

Flink, A. E., Noormets, R., Kirchner, N., Benn, D. I., Luckman, A., & Lovell, H. (2015). The evolution of a submarine landform record following recent and multiple surges of tunabreen glacier, svalbard. *Quaternary Science Reviews*, *108*, 37–50.

Flowers, G. E. (2015). Modelling water flow under glaciers and ice sheets. *Proceedings of the Royal Society A: Mathematical, Physical and Engineering Sciences*, *471*(2176), 20140907.

Flowers, G. E., & Clarke, G. (2002a). A multicomponent coupled model of glacier hydrology, 1, Theory and synthetic examples. *Journal Geophys. Res.*, *107*(B11), 2287.

Flowers, G. E., & Clarke, G. (2002b). A multicomponent coupled model of glacier hydrology, 2, Application to Trapridge Glacier, Yukon, Canada. *Journal Geophys. Res.*, *107*(B11), 2288.

Fowler, A. (1987). A theory of glacier surges. *Journal of Geophysical Research: Solid Earth (1978–2012)*, *92*(B9), 9111–9120.

Fowler, A. (1989). A mathematical analysis of glacier surges. *SIAM J. Appl. Math.*, *49*(1), 246-263.

Gagliardini, O., Cohen, D., Råback, P., & Zwinger, T. (2007). Finite-element modeling of subglacial cavities and related friction law. *Journal of Geophysical Research: Earth Surface (2003–2012)*, *112*(F2).

Gagliardini, O., Zwinger, T., Gillet-Chaulet, F., Durand, G., Favier, L., Fleurian, B. d., et al. (2013). Capabilities and performance of Elmer/Ice, a new-generation ice sheet model. *Geoscientific Model Development*, *6*(4), 1299–1318.

Geudtner, D., Torres, R., Snoeij, P., Davidson, M., & Rommen, B. (2014). Sentinel-1 system capabilities and applications. In *Geoscience and Remote Sensing Symposium (IGARSS), 2014 IEEE International* (pp. 1457–1460).

Glen, J. W. (1955). The creep of polycrystalline ice. In *Proceedings of the royal society of london a: Mathematical, physical and engineering sciences* (Vol. 228, pp. 519–538).

Goelzer, H., Robinson, A., Seroussi, H., & Van De Wal, R. S. (2017). Recent progress in greenland ice sheet modelling. *Current climate change reports*, *3*(4), 291–302.

Goward, S. N., Masek, J. G., Williams, D. L., Irons, J. R., & Thompson, R. (2001). The Landsat 7 mission: Terrestrial research and applications for the 21st century. *Remote Sensing of Environment*, *78*(1-2), 3–12.

Greve, R., & Blatter, H. (2009). *Dynamics of Ice Sheets and Glaciers.* Berlin, Germany etc.: Springer.

Gudmundsson, G. H. (2003). Transmission of basal variability to a glacier surface. *Journal of Geophysical Research: Solid Earth*, *108*(B5).

Gulley, J., Benn, D., Screaton, E., & Martin, J. (2009). Mechanisms of englacial conduit formation and their implications for subglacial recharge. *Quaternary Science Reviews*, *28*(19-20), 1984–1999.

Gulley, J., Grabiec, M., Martin, J., Jania, J., Catania, G., & Glowacki, P. (2012). The effect of discrete recharge by moulins and heterogeneity in flow-path efficiency at glacier beds on subglacial hydrology. *Journal of Glaciology*, *58*(211), 926–940.

Haga, O. N., McNabb, R., Nuth, C., Altena, B., Schellenberger, T., & Kääb, A. (2020). From high friction zone to frontal collapse: dynamics of an ongoing tidewater glacier surge, negribreen, svalbard. *Journal of Glaciology*, *66*(259), 742–754.

Hallet, B. (1981). Glacial abrasion and sliding: their dependence on the debris concentration in basal ice. *Annals of Glaciology*, *2*, 23–28.

Hambrey, M. J., & Dowdeswell, J. A. (1997). Structural evolution of a surge-type polythermal glacier: Hessbreen, svalbard. *Annals of Glaciology*, *24*, 375–381.

Hamilton, G. S., & Dowdeswell, J. A. (1996). Controls on glacier surging in svalbard. *Journal of Glaciology*, *42*(140), 157–168.

Hansen, S. (2003). From surge-type to non-surge-type glacier behaviour: midre lovenbreen, svalbard. *Annals of Glaciology*, *36*, 97–102.

Harrison, W., & Post, A. (2003). How much do we really know about glacier surging? *Annals of Glaciology*, *36*(1), 1–6.

Heinrichs, T. A., Mayo, L., Echelmeyer, K., & Harrison, W. (1996). Quiescent-phase evolution of a surge-type glacier: Black Rapids Glacier, Alaska, USA. *Journal of Glaciology*, *42*(140), 110–122.

Helm, V., Humbert, A., & Miller, H. (2014). Elevation and elevation change of Greenland and Antarctica derived from CryoSat-2. *The Cryosphere*, *8*(4), 1539–1559.

Herzfeld, U. C. (1998). *The 1993-1995 surge of bering glacier (Alaska) — a photographic documentation of crevasse patterns and environmental changes* (Vol. 17). Geograph. Gesellschaft Trier and Fachbereich VI – Geographie/Geowissenschaften, Universität Trier.

Herzfeld, U. C. (2004). *Atlas of Antarctica: Topographic maps from geostatistical analysis of satellite radar altimeter data* (Vol. 1). Springer Verlag.

Herzfeld, U. C., Clarke, G. K. C., Mayer, H., & Greve, R. (2004). Derivation of deformation characteristics in fast-moving glaciers. *Computers & Geosciences*, *30*(3), 291–302.

Herzfeld, U. C., Lawson, M., Trantow, T., & Nylen, T. (2022). Airborne validation of icesat-2 atlas data over crevassed surfaces and other complex glacial environments: Results from experiments of laser altimeter and kinematic gps data collection from a helicopter over a surging arctic glacier (negribreen, svalbard). *Remote Sensing*, *14*(5), 1185.

Herzfeld, U. C., Lingle, C. S., & Lee, L. (1993). Geostatistical evaluation of satellite radar altimetry for high resolution mapping of Antarctic ice streams. *Annals Glaciol.*, *17*, 77-85.

Herzfeld, U. C., & Mayer, H. (1997). Surge of Bering Glacier and Bagley Ice Field, Alaska: an update to August 1995 and an interpretation of brittle-deformation patterns. *Journal of Glaciology*, *43*(145), 427–434.

Herzfeld, U. C., McDonald, B., Stachura, M., Hale, R. G., Chen, P., & Trantow, T. (2013). Bering Glacier surge 2011: Analysis of laser altimeter data. *Annals of Glaciology*, *54(63)*, 158–170.

Herzfeld, U. C., McDonald, B., & Weltman, A. (2013). Bering Glacier and Bagley Ice Valley surge 2011: Crevasse classification as an approach to map deformation stages and surge progression. *Annals of Glaciology*, *54(63)*, 279–286.

Hill, E. A., Carr, J. R., & Stokes, C. R. (2017). A review of recent changes in major marine-terminating outlet glaciers in northern greenland. *Frontiers in Earth Science*, *4*, 111.

Hindmarsh, R. (2004). A numerical comparison of approximations to the Stokes equations used in ice sheet and glacier modeling. *Journal of Geophysical Research: Earth Surface*, *109*(F1).

Hooke, R. L. (1981). Flow law for polycrystalline ice in glaciers: comparison of theoretical predictions, laboratory data, and field measurements. *Reviews of Geophysics*, *19*(4), 664–672.

Humphrey, N. F., & Raymond, C. (1994). Hydrology, erosion and sediment production in a surging glacier: Variegated Glacier, Alaska, 1982–83. *Journal of Glaciology*, *40*(136), 539–552.

Huss, M. (2013). Density assumptions for converting geodetic glacier volume change to mass change. *The Cryosphere*, *7*(3), 877–887.

Hutter, K. (2017). *Theoretical glaciology: Material science of ice and the mechanics of glaciers and ice sheets* (Vol. 1). Springer.

Iken, A. (1981). The effect of the subglacial water pressure on the sliding velocity of a glacier in an idealized numerical model. *Journal of Glaciology*, *27*(97), 407–421.

Iverson, N. R., Cohen, D., Hooyer, T. S., Fischer, U. H., Jackson, M., Moore, P. L., et al. (2003). Effects of basal debris on glacier flow. *Science*, *301*(5629), 81–84.

Jansson, P., Hock, R., & Schneider, T. (2003). The concept of glacier storage: a review. *Journal of Hydrology*, *282*(1-4), 116–129.

Jay-Allemand, M., Gillet-Chaulet, F., Gagliardini, O., & Nodet, M. (2011a). Investigating changes in basal conditions of Variegated Glacier prior to and during its 1982-1983 surge. *The Cryosphere*, *5*(3), 659–672.

Jay-Allemand, M., Gillet-Chaulet, F., Gagliardini, O., & Nodet, M. (2011b). Investigating changes in basal conditions of Variegated Glacier prior to and during its 1982-1983 surge. *The Cryosphere*, *5*(3), 659–672. Retrieved from http://www.the-cryosphere.net/5/659/2011/

Jiskoot, H. (1999). Characteristics of surge-type glaciers. *Ph.D. thesis*, 1-262.

Jiskoot, H. (2011). Glacier surging. *Encyclopedia of Snow, Ice and Glaciers*, 415–428.

Jiskoot, H., Murray, T., & Boyle, P. (2000). Controls on the distribution of surge-type glaciers in svalbard. *Journal of Glaciology*, *46*(154), 412–422.

Jiskoot, H., Murray, T., & Luckman, A. (2003). Surge potential and drainage-basin characteristics in East Greenland. *Annals of Glaciology*, *36*, 142–148.

Josberger, E. G., Shuchman, R. A., Meadows, G. A., Savage, S., & Payne, J. (2010). Hydrography and circulation of ice-marginal lakes at Bering Glacier, Alaska, USA. *Geological Society of America Special Paper*(462), 67–82.

Kamb, B. (1970). Sliding motion of glaciers: theory and observation. *Reviews of Geophysics*, *8*(4), 673–728.

Kamb, B., & Engelhardt, H. (1987). Waves of accelerated motion in a glacier approaching surge: the mini-surges of variegated glacier, alaska, usa. *Journal of Glaciology*, *33*(113), 27–46.

Kamb, W., Raymond, C., Harrison, W., Engelhardt, H., Echelmeyer, K., Humphrey, N., et al. (1985). Glacier surge mechanism: 1982-1983 surge of Variegated Glacier, Alaska. *Science*, *227*(4686), 469-479.

Kamb, W. B. (1987). Glacier Surge Mechanism Based on Linked Cavity Configuration of the Basal Water Conduit System. *Journal Geophys. Res.*, *92*(B9), 9083-9100.

King, M. D., Howat, I. M., Candela, S. G., Noh, M. J., Jeong, S., Noël, B. P., et al. (2020). Dynamic ice loss from the greenland ice sheet driven by sustained glacier retreat. *Communications Earth & Environment*, *1*(1), 1–7.

Koehler, R., & Carver, G. (2018). Active faults and seismic hazards in Alaska. *Alaska Div. Geol. Geophys. Surv., Miscellaneous Publication 160*.

Larsen, C., Burgess, E., Arendt, A., O'neel, S., Johnson, A., & Kienholz, C. (2015). Surface melt dominates Alaska glacier mass balance. *Geophysical Research Letters*, *42*(14), 5902–5908.

LeBlanc, L. (2009). *Icequakes and ice motion: A time-series analysis of the dynamics of the Bering Glacier, Alaska.* Unpublished doctoral dissertation, University of Alaska Fairbanks.

Lefauconnier, B., & Hagen, J. O. (1991). Surging and calving glaciers in Eastern Svalbard. *Meddeleslser*(116), 133.

Le Meur, E., Gagliardini, O., Zwinger, T., & Ruokolainen, J. (2004). Glacier flow modelling: a comparison of the shallow ice approximation and the full-stokes solution. *Comptes Rendus Physique*, *5*(7), 709–722.

Lingle, C., & Fatland, D. (2003). Does englacial water storage drive temperate glacier surges? *Annals of Glaciology*, *36*, 14–20.

Lingle, C., Post, A., Herzfeld, U. C., Molnia, B. F., Krimmel, R., & Roush, J. (1993). Bering Glacier surge and iceberg-calving mechanism at Vitus Lake, Alaska, USA. *Journal of Glaciology*, *39*, 722–727.

Lliboutry, L. (1968). General theory of subglacial cavitation and sliding of temperate glaciers. *Journal of Glaciology*, *7*, 21–58.

Magnússon, E., Björnsson, H., Rott, H., & Pálsson, F. (2010). Reduced glacier sliding caused by persistent drainage from a subglacial lake. *The Cryosphere*, *4*(1), 13–20.

Mansell, D., Luckman, A., & Murray, T. (2012). Dynamics of tidewater surge-type glaciers in northwest svalbard. *Journal of Glaciology*, *58*(207), 110–118.

Markham, B. L., Storey, J. C., Williams, D. L., & Irons, J. R. (2004). Landsat sensor performance: History and current status. *IEEE Transactions on Geoscience and Remote Sensing*, *42*(12), 2691–2694.

Mayer, H., & Herzfeld, U. (2000). Structural glaciology of the fast-moving Jakobshavn Isbræ, Greenland, compared to the surging Bering Glacier, Alaska, USA. *Annals of Glaciology*, *30*(1), 243–249.

Meier, M., & Post, A. (1969). What are glacier surges? *Canadian Journal of Earth Sciences*, *6*(4), 807–817.

Meier, M., & Post, A. (1987). Fast tidewater glaciers. *Journal of Geophysical Research: Solid Earth (1978–2012)*, *92*(B9), 9051–9058.

Messerli, A., & Grinsted, A. (2015). Image georectification and feature tracking toolbox: ImGRAFT. *Geoscientific Instrumentation, Methods and Data Systems*, *4*(1), 23.

Molnia, B., & Post, A. (1995). Holocene history of Bering Glacier, Alaska: A prelude to the 1993-1994 surge. *Physical Geography*, *16*(2), 87–117.

Molnia, B., & Williams, R. (2001). *Glaciers of Alaska* (Vol. 28-2). Alaska Geographic Society.

Molnia, B. F. (2008). *Alaska.* Washington, D.C.: U.S. Geological Survey Professional Paper 1386-K.

Molnia, B. F., & Post, A. (2010a). Introduction to the Bering Glacier system, Alaska/Canada: Early Observations and scientific investigations, and key geographic features. *Geological Society of America Special Paper*(462), 13–42.

Molnia, B. F., & Post, A. (2010b). Surges of the Bering Glacier. *Bering Glacier: interdisciplinary studies of Earth's largest temperate surging glacier*, 291–314.

Murray, T., & Porter, P. R. (2001). Basal conditions beneath a soft-bedded polythermal surge-type glacier: Bakaninbreen, svalbard. *Quaternary International*, *86*(1), 103–116.

Murray, T., Strozzi, T., Luckman, A., Jiskoot, H., & Christakos, P. (2003). Is there a single surge mechanism? Contrasts in dynamics between glacier surges in Svalbard and other regions. *Journal of Geophysical Research: Solid Earth*, *108*(B5).

Nuttall, A.-M., & Hodgkins, R. (2005). Temporal variations in flow velocity at finsterwalderbreen, a svalbard surge-type glacier. *Annals of Glaciology*, *42*, 71–76.

Pörtner, H.-O., Roberts, D. C., & Masson-Delmotte, V. (2022). *The ocean and cryosphere in a changing climate: Special report of the intergovernmental panel on climate change.* Cambridge University Press.

Post, A. (1972). Periodic surge origin of folded medial moraines on Bering Piedmont Glacier, Alaska. *Journal of Glaciology*, *11*(62), 219-226.

Raymond, C. (1987). How do glaciers surge? A review. *Journal of Geophysical Research*, *92*(B9), 9121–9134.

Raymond, C. (1988). Evolution of Variegated Glacier, Alaska, USA, prior to its surge. *J. Glaciol*, *34*(117), 154–169.

Raymond, C., Benedict, R., Harrison, W., Echelmeyer, K., & Sturm, M. (1995). Hydrological discharges and motion of Fels and Black Rapids Glaciers, Alaska, USA: implications for the structure of their drainage systems. *Journal of Glaciology*, *41*(138), 290–304.

Raymond, C., Johannesson, T., Pfeffer, T., & Sharp, M. (1987). Propagation of a glacier surge into stagnant ice. *Journal of Geophysical Research: Solid Earth*, *92*(B9), 9037–9049.

Rignot, E., & Kanagaratnam, P. (2006). Changes in the velocity structure of the greenland ice sheet. *Science*, *311*(5763), 986–990.

Rignot, E., Mouginot, J., Larsen, C., Gim, Y., & Kirchner, D. (2013). Low-frequency radar sounding of temperate ice masses in Southern Alaska. *Geophysical Research Letters*, *40*(20), 5399–5405.

Robin, G. d. Q. (1969). Initiation of glacier surges. *Canadian Journal of Earth Sciences*, *6*(4), 919–928.

Robin, G. d. Q., & Weertman, J. (1973). Cyclic surging of glaciers. *Journal of Glaciology*, *12*(64), 3–18.

Roush, J. J., Lingle, C. S., Guritz, R. M., Fatland, D. R., & Voronina, V. A. (2003). Surge-front propagation and velocities during the early-1993-95 surge of Berring Glacier, Alaska, U.S.A., from sequential SAR imagery. *Annals of Glaciology*, *36*, 37–44.

Roy, D. P., Wulder, M., Loveland, T. R., Woodcock, C., Allen, R., Anderson, M., et al. (2014). Landsat-8: Science and product vision for terrestrial global change research. *Remote sensing of Environment*, *145*, 154–172.

Schoof, C. (2005). The effect of cavitation on glacier sliding. *Proc. R. Soc. A*, *461*, 609-627.

Sevestre, H., Benn, D. I., Hulton, N. R., & Bælum, K. (2015). Thermal structure of Svalbard glaciers and implications for thermal switch models of glacier surging. *Journal of Geophysical Research: Earth Surface*, *120*(10), 2220–2236.

Sharp, M., Richards, K., Willis, I., Arnold, N., Nienow, P., Lawson, W., et al. (1993). Geometry, bed topography and drainage system structure of the haut glacier d'arolla, switzerland. *Earth Surface Processes and Landforms*, *18*(6), 557–571.

Sharp, R. P. (1951). Features of the firn on upper seward glacier st. elias mountains, canada. *The Journal of Geology*, *59*(6), 599–621.

Shoemaker, E., & Leung, H. (1987). Subglacial drainage for an ice sheet resting upon a layered deformable bed. *Journal of Geophysical Research: Solid Earth*, *92*(B6), 4935–4946.

Shreve, R. (1972). Movement of water in glaciers. *Journal of Glaciology*, *11*(62), 205–214.

Shuchman, R., & Josberger, E. G. (2010). Bering Glacier: Interdisciplinary Studies of Earth's Largest Temperate Glacier. *Geological Society of America Special Paper*(462), 384.

Shuchman, R. A., Josberger, E. G., Jenkins, L. K., Payne, J. F., Hatt, C. R., & Spaete, L. (2010). Remote sensing of the Bering Glacier region. *Geological Society of America Special Paper*(462), 43–66.

Solgaard, A., Simonsen, S., Grinsted, A., Mottram, R., Karlsson, N., Hansen, K., et al. (2020). Hagen bræ: A surging glacier in north greenland—35 years of observations. *Geophysical research letters*, *47*(6), e2019GL085802.

Sund, M., Eiken, T., Hagen, J. O., & Kääb, A. (2009). Svalbard surge dynamics derived from geometric changes. *Annals of Glaciology*, *50*(52), 50–60.

Sund, M., Lauknes, T., & Eiken, T. (2014). Surges in the Nathorstbreen glacier system, Svalbard. *The Cryosphere*, *8*(2), 623–638.

Tangborn, W. (2013). Mass balance, runoff and surges of Bering Glacier, Alaska. *The Cryosphere*, *7*(3), 867–875.

Trantow, T. (2014). *Numerical experiments of dynamical processes during the 2011-2013 surge of the Bering-Bagley Glacier System, using a full-Stokes finite element model*. Unpublished master's thesis, University of Colorado.

Trantow, T. (2020). *Surging in the bering-bagley glacier system, alaska – understanding glacial acceleration through new methods in remote sensing, numerical modeling and model-data comparison.* Unpublished doctoral dissertation, University of Colorado.

Trantow, T., & Herzfeld, U. (2016). Spatiotemporal mapping of a large mountain glacier from CryoSat-2 altimeter data: surface elevation and elevation change of Bering Glacier during surge (2011-2014). *International Journal of Remote Sensing*, 0-28.

Trantow, T., & Herzfeld, U. C. (2018). Crevasses as indicators of surge dynamics in the Bering Bagley Glacier System, Alaska: Numerical experiments and comparison to image data analysis. *Journal of Geophysical Research: Earth Surface*.

Trantow, T., Herzfeld, U. C., Helm, V., & Nilsson, J. (2020). Sensitivity of glacier elevation analysis and numerical modeling to cryosat-2 siral retracking techniques. *Computers & Geosciences*, 104610.

Truffer, M., Harrison, W. D., & Echelmeyer, K. A. (2000). Glacier motion dominated by processes deep in underlying till. *Journal of Glaciology*, *46*(153), 213–221.

Turrin, J., Forster, R. R., Larsen, C., & Sauber, J. (2013). The propagation of a surge front on Bering Glacier, Alaska, 2001-2011. *Annals of Glaciology*, *54*(63).

Veci, L., Prats-Iraola, P., Scheiber, R., Collard, F., Fomferra, N., & Engdahl, M. (2014). The Sentinel-1 toolbox. In *Proceedings of the ieee international geoscience and remote sensing symposium (igarss)* (pp. 1–3).

Wingham, D. J., Francis, C. R., Baker, S., Bouzinac, C., Cullen, R., Chateau-Thierry, P. de, et al. (2006). CryoSat: A Mission to Determine the Fluctuations in Earth's Land and Marine Ice Fields. *Advances in Space Research*, 841-871.

Woodward, J., Murray, T., & McCaig, A. (2002). Formation and reorientation of structure in the surge-type glacier kongsvegen, svalbard. *Journal of Quaternary Science: Published for the Quaternary Research Association*, *17*(3), 201–209.